DEVELOPING A COMPUTATIONAL MODEL OF THE PILOT'S BEST POSSIBLE EXPECTATION OF AIRCRAFT STATE GIVEN VESTIBULAR AND VISUAL CUES

A Thesis
Presented to
The Academic Faculty

by

Can Onur

In Partial Fulfillment
of the Requirements for the Degree
Master of Science in the
School of Aerospace Engineering

Georgia Institute of Technology
December 2014

DEVELOPING A COMPUTATIONAL MODEL OF THE PILOT'S BEST POSSIBLE EXPECTATION OF AIRCRAFT STATE GIVEN VESTIBULAR AND VISUAL CUES

Approved by:

Dr. Amy Pritchett, Advisor
School of Aerospace Engineering
Georgia Institute of Technology

Dr. Eric Johnson
School of Aerospace Engineering
Georgia Institute of Technology

Dr. Santosh Mathan
Human Centered Systems
Honeywell Laboratories

Date Approved: November 24, 2014

ACKNOWLEDGEMENTS

I would like start by expressing my sincere gratitude to my advisor, Dr. Amy Pritchett, for giving me the opportunity to be in a lab that has members from all over the world. It was a thrill to become a part of this culturally diverse and wonderful community.

I also want to acknowledge the support of my committee members, Dr. Santosh Mathan, and Dr. Eric Johnson. I would like to thank them for serving on my committee and devoting their time to help me with the thesis.

My friends have had a substantial impact on everything I have learned and experienced while at Georgia Tech. I feel like I should have learned more French though. I would like to express my gratitude to Adrien, Anil, Antoine, Aparna, Arvind, Benjamin, David, Gabriel, Guliz, Raunak, Sebastien, Vlad and all the other unlisted friends. Special thanks are due to my project mate, Anil, for being a great companion on this tough but fun journey.

Finally, I would like to thank Murat, Aysin, Olga and Gioia. They never stopped supporting me via telecommunication applications. Without them, I would not have succeeded.

TABLE OF CONTENTS

LIST OF TABLES

LIST OF FIGURES

SUMMARY

Loss of Control (LOC) accidents are a major threat for aviation, and contribute the highest risk for fatalities in all aviation accidents. The major contributor to LOC accidents is pilot spatial disorientation (SD), which accounts for roughly 32% of all LOC accidents. A pilot experiences SD during flight when the pilot's expectation of the aircraft's state deviates from reality. This deviation results from a number of underlying mechanisms, such as distraction, failure to monitor flight instruments, and vestibular illusions. Previous researchers have developed computational models to understand those mechanisms. However, these models are limited in scope as they do not model the pilot's knowledge of the aircraft dynamics. This research proposes a novel model to predict the best-possible-pilot-expectation of the aircraft state given vestibular and visual cues. The proposed model uses a Model-Based Observer (MBO) as the infrastructure needed to establish an "expert" pilot. Expert pilots are known to form an internal model of the operated system through training and experience, which allows the expert to generate better internal expectations of the system states. Pilots' internal expectations are enhanced by the presence of information fed through the pilots' sensory systems. Thus, the proposed model integrates pilot's knowledge of the system dynamics (i.e. an aircraft model) with a continuous vestibular sensory model and a discrete visual-sampling sensory model. The computational model serves to investigate the underlying mechanisms of SD during flight and provide a quantitative analysis tool to support flight deck and countermeasure designs.

CHAPTER 1

INTRODUCTION

1.1 Motivation

Loss of Control (LOC) accidents are still the most significant threat to both commercial air transport and general aviation, and are the type of accidents with the highest risk for fatalities. For commercial jet transports, it is estimated that about 0.3 fatal LOC accidents occur per million departures [1]. There are a number of contributors to LOC accidents, but spatial disorientation makes up 32% of all LOC accidents, making it the primary contributing factor to the human-related aircraft incidents/accidents [2-4]. (Figure 1)

Spatial orientation is defined as the ability to perceive motion and three-dimensional position and attitude in relation to the surrounding environment. Conversely, spatial disorientation (SD) occurs when a pilot fails to properly sense the aircraft's motion, position or attitude. Unfortunately, the possibility for a pilot to experience SD during his/her career is on the order of 90-100 percent [5-7]. If the SD is not recognized quickly, it can lead to LOC.
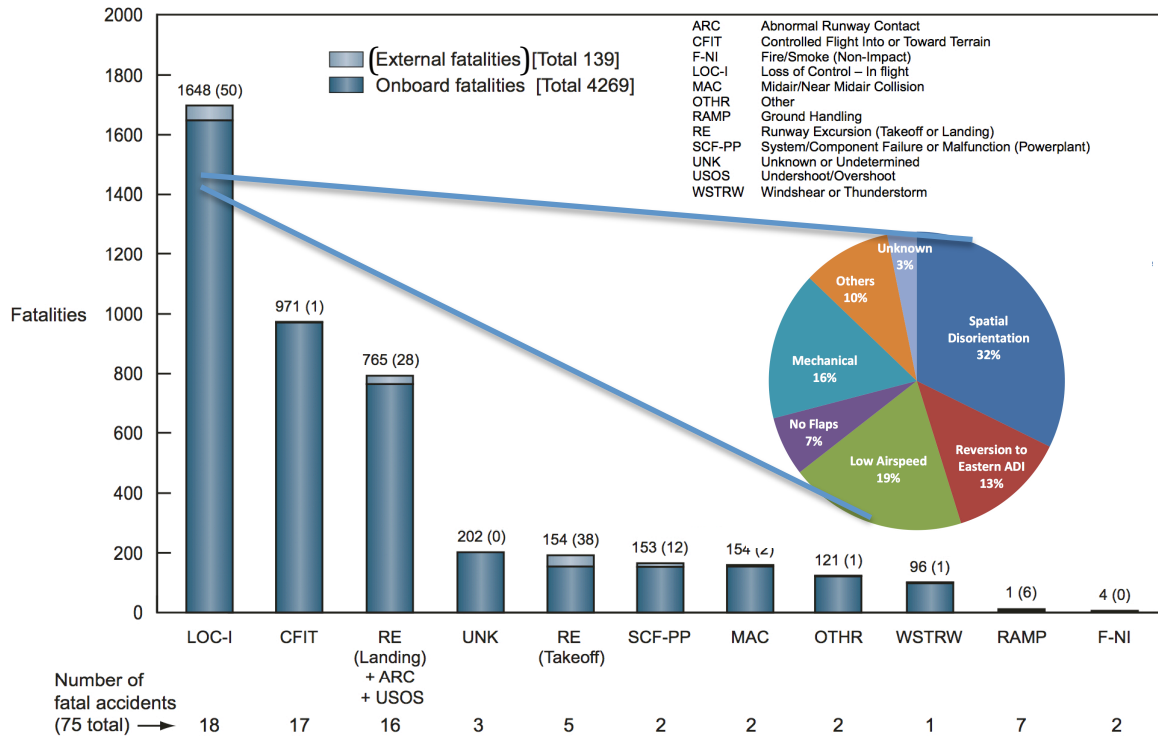
Figure 1: LOC as a primary cause of fatalities in aviation [1-2]

Humans primarily sense their orientation through two sensory systems: the visual and the vestibular system [27]. The vestibular system is located in the inner ear and consists of two parts: the *otoliths* detect linear motion and the *Semi-Circular Canals* (SCC) detect angular motion. The human vestibular system evolved in a 1-g, low speed environment, which makes it capable of perceiving motions during actions such as walking, sitting etc. However, the vestibular system is easy to trick in flight.

The limits of the vestibular system can be compensated for by visual reference. However, out-of-the-window visual reference might not always be available to the pilot (night-time flight, foggy weather, in the clouds). According to a 1954 study, the average life expectancy of a non-instrument-rated pilot who flies into clouds or instrument meteorological conditions (IMC) is 178 seconds from the onset of LOC due to SD [8]. This demands proper visual scans of the flight instruments.

Additionally, knowledge of the aircraft dynamics plays a substantial role in pilot's expectation of the aircraft states. To make more realistic quantitative assessments about state of the aircraft, sensory system information should be integrated with the pilot's knowledge and experience of the dynamics of the aircraft (assuming that the pilot has enough knowledge and experience through his/her training and previous flight-hours). For these purposes, a Model-Based Observer (MBO) can be developed to establish the infrastructure needed to actively integrate the information coming from the major sensory systems (i.e., vestibular and visual systems) with the pilot's internal expectations of the state of the aircraft. Out of this model, an expert pilot's best possible expectation can be estimated.

Many studies have sought to find feasible countermeasures to SD-related accidents and incidents [9]. There is a wide range of proposed SD countermeasures including training programs, auditory and tactile alerting systems, and flight deck instrument improvements. Most of these countermeasures are designed to attract the pilot's attention to flight deck displays instead of relying on his/her vestibular sensing. However, current quantitative tools are insufficient to assess a flight deck display design [10]. A quantitative assessment should be able to predict the pilot's potential awareness and expectation of energy-state and attitude during the course of a flight. Such predictions can then serve to identify critical information requirements for the pilot to form an accurate expectation of the aircraft states.

1.2 Objectives

The goal of this thesis work is to develop a computational model to predict a pilot's best possible expectation of aircraft state given vestibular and visual cues, both to investigate the underlying mechanisms of spatial disorientation (SD) during flight and to provide a quantitative analysis tool for flight deck design as a countermeasure to SD. This goal is supported by two objectives. The first objective is to develop a

computational model (using a Model-Based Observer) to predict pilot's expectation of the aircraft state given vestibular and visual cues (measurements). The second objective is the parameterization, verification and validation of the model using previously studied scenarios.

1.3 Overview of the Thesis

Chapter 2 describes the background of the problem and previous work that relates to this thesis. It concludes with a discussion of a need for a new model. The following chapters, Chapter 3 & 4, are dedicated to the objectives of the thesis: Chapter 3 explains the development of the model and describes the structure in-depth; Chapter 4 starts with a discussion on the parameterization of the model and concludes with the validation and verification of the proposed model based on the previous studies and empirical results from the literature. Finally, Chapter 5 summarizes the thesis work and lists its potential contributions.

CHAPTER 2

BACKGROUND

This chapter discusses the previous studies relevant to this thesis work. It starts with a discussion of the pilot's expectation of orientation and factors contributing to this expectation. This first section discusses the impact of vestibular sensors, visual sensors, and pilot's knowledge of the aircraft dynamics on pilot expectation. The discussion of pilot knowledge reviews the structure of the Model-Based Observer (MBO), how it can be used as an expert pilot to predict the best possible pilot expectation, and various former models that have been developed using this approach.

The second section continues with discussion of sensory system models needed for the proposed model together as available in the existing literature. This section starts with the background section, describing the chronological development of vestibular models in the literature. The following section discusses the sensory dynamics of those models to identify most relevant model to be used in this thesis.

Finally, this chapter concludes with a discussion on the current orientation models to highlight the need for a novel model.

2.1 Contributions to Pilot Expectation

Human orientation sensing happens primarily through two sensory systems: the visual and the vestibular system. A third contributor to orientation sensation is the proprioceptive system, which provides information about the relative motion and orientation of the body parts through special sense organs (pressure receptors) in the muscles, tendons, and joints [28]. Both the otolith sensors (part of the vestibular system) and the proprioceptive pressure receptors detect the inertial forces due to linear acceleration. They can be considered as redundant sensors that increase the accuracy of

the orientation sensation. However, forces experienced during flight maneuvers be perceived erroneously by these pressure receptors alone [12]. Therefore, this thesis work utilizes the primary orientation sensors, namely the vestibular and the visual sensory systems.

The human vestibular system is capable of proper sensing during natural motions like walking, sitting, running, etc. However, it can cause illusions in flight when the body experiences maneuvers such as slow rolls or sustained forward accelerations. Therefore, visual sampling of the outside view or the flight instruments is a vital correction to vestibular sensing. Pilot knowledge of the aircraft dynamics can also contribute to expectation. The pilot's expertise allows him/her to project the orientation of the aircraft based on the control inputs applied to the aircraft. Thus, the following three sections talk about these three contributions to pilot expectation: vestibular, visual, and pilot knowledge of the aircraft dynamics.

2.1.1 Vestibular Inputs

Located in the inner ear, the vestibular system contributes to sensation of balance. It is mainly responsible for self-motion perception and is a building block of the postural control mechanism [29]. The vestibular system's perception of linear and angular acceleration provides the continuous, unconscious sensation of spatial orientation [16]. Its two components help perceive both angular and linear motion. The first component, the semi-circular canal (SCC), is responsible for angular motion perception. The second component, otoliths, is responsible for linear motion perception and provides Gravito-Inertial Force (GIF) measurements (specific force).

Most vestibular models include semi-circular canal (SCC) dynamics for angular motion sensation and the otolith dynamics to sense the gravito-inertial forces (GIF) [12-14 & 18-22]. They provide the specific outputs shown in Figure 2. The SCC is modeled as a torsion pendulum with some additional rate sensitivity and adaptation. It acts as an

6

angular rate sensor that takes the angular velocity components as input and outputs afferent firing rates that represents measures of angular velocity. However, at high and low frequencies afferent firing rate response diverges from angular velocity. This issue was resolved by augmenting the basic torsion model with two components: Phase lead at low frequencies, and a lead component to reproduce the high-frequency deviations [30]. The otoliths are modeled as a mechanical accelerometer with some additional rate sensitivity. They take GIF (specific force) as an input and output the afferent firing rates corresponding to perception of GIF. Detailed discussion of the vestibular sensor dynamics can be found in the following section (*2.2 The Vestibular System Models*).

Vestibular System

SCC

Otolith

$$p$$
$$q$$
$$r$$

$$-\theta \cdot g_z - \dot{u}$$
$$\phi \cdot g_z - \dot{v}$$
$$g_z - \dot{w}$$

Figure 2: *Vestibular system outputs*

The vestibular system cannot sense the motion/orientation that is below a threshold value on angular velocity. Such sub-threshold maneuvers require special consideration in models of spatial disorientation, especially in commercial aviation, where some autopilots intentionally perform sub-threshold maneuvers for the sake of passenger comfort.

Many empirical studies have examined these threshold values. The general results are summarized by Mulder's Law, which defines the angular perception threshold for transient accelerations (<10s). According to Mulder's Law, the product of the angular acceleration magnitude and the maneuver duration should be at least 2.5 deg/s for the SCC to sense the maneuver. For sustained turns, this threshold value drops down to 0.5 deg/s [31]. The otolith's linear motion perception thresholds have been studied by

Guedry. Guedry's empirical studies showed that the mean roll and pitch axes threshold is 0.06 m/s^2. These threshold values allow maneuvers to be categorized as either above or sub-threshold [12].

Especially in the aviation context, the vestibular system is prone to providing false inputs and, thus, causing illusions in the absence of a proper visual scanning. Prolonged maneuvers, constantly changing accelerations, and a wide range of maneuver rates can cause illusions and, thus, misinterpretation of the actual orientation [12-21]. The most common vestibular illusions include (1) somatogyral illusion caused by the limitations of the SCC, and (2) somatogravic illusions caused by the limitation of the otolith as described in the following two sub-sections [32].

2.1.1.1 Somatogyral Illusions

Somatogyral illusions occur due to the sensory dynamics and limitations of the angular rate sensors, namely the SCC. Their threshold values inhibit the sensation of sub-threshold motions. Additionally, SCC afferent signals tend to die out in a sustained maneuver. A common example of a somatogyral illusion is called the "leans", in which a sub-threshold bank maneuver is followed by an above-threshold banking maneuver (Figure 3). Experiencing consecutive sub-threshold and above-threshold maneuvers causes incoherent perception of the orientation if not corrected by visual scans.

Pilot allows wing to drop at a sub-threshold rate

Pilot detects attitude error from instruments and returns to wings level at a supra-threshold rate

Pilot aligns head and trunk with perceived vertical and leans to right

Pilot's Actual Gravitational vertical

Perceived pilot relationship to vertical
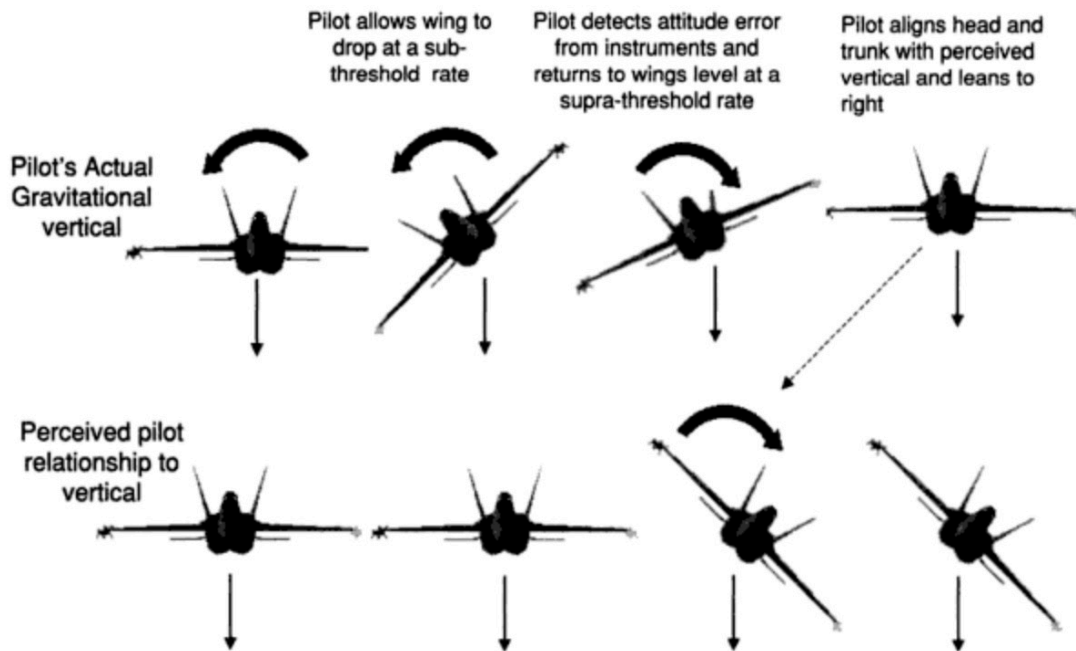
Figure 3: *Somatogyral Illusion (Leans) – common example of pilot disorientation due to SCC thresholds [12]*

Some previous orientation models have been able to capture this illusion. For example, Borah et al.'s model captures the SCC response that dies out in case of a sustained stimulus (Figure 4).
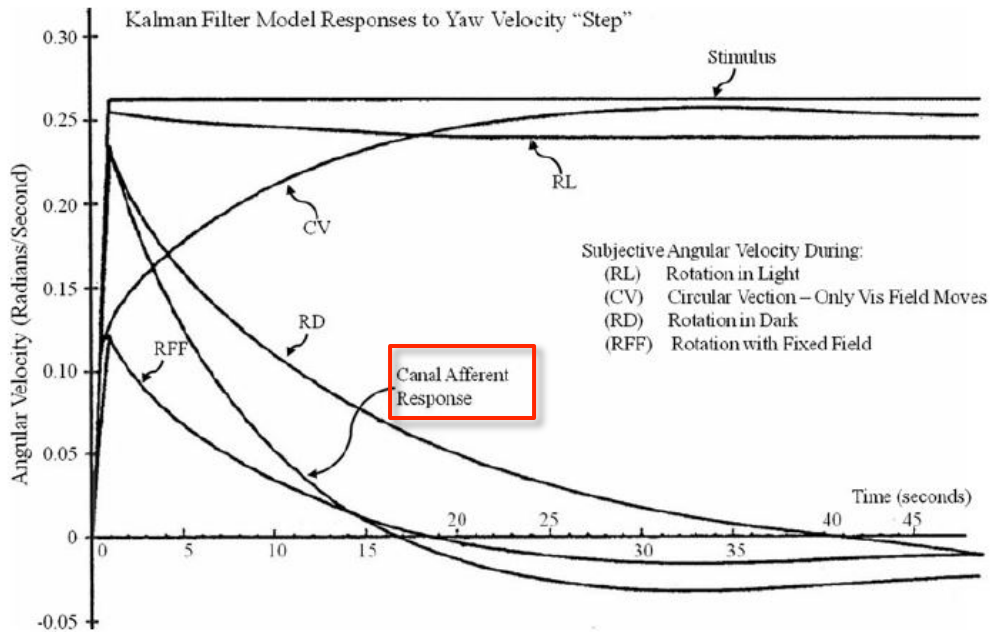
Figure 4: *Borah et al.'s orientation model response to a step angular velocity stimulus. The SCC model output is highlighted [18]*

2.1.1.2 Somatogravic Illusions

One of the most common somatogravic illusions is the "pitch-up" sensation that occurs in the case of a linear forward acceleration (Figure 5). In the extreme example of a catapult take-off from an aircraft carrier, the pilot experiences an approximately 4g pulse linear forward acceleration that lasts 2-3 seconds, yet the pilot senses a persistent pitching-up illusion for about 30 seconds afterwards [33]. In commercial air transport, nighttime take-offs and go-arounds are considered to be critical in terms of somatogravic illusions [12]. Thus, the somatogravic illusion is considered to be a significant contributor to the spatial disorientation accidents. It was reported that between 1979 and 1993, 35 accidents in Australia occurred at night during the take-off phase [7].
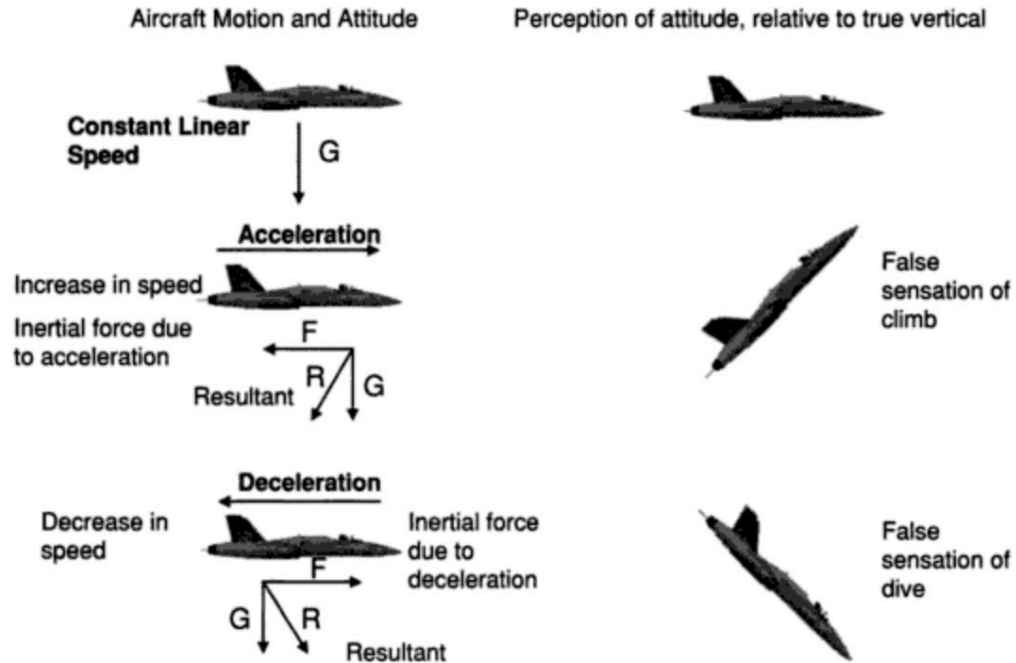
Figure 5: *False sensation of pitch during linear acceleration/deceleration [12]*

There are currently some computational models that capture the somatogravic illusion. For instance, Pommellet's orientation model captures the somatogravic illusion during a 0.2g step acceleration maneuver, in which the pilot sensation deviates from zero pitch angle to a positive pitch angle value (Figure 6).
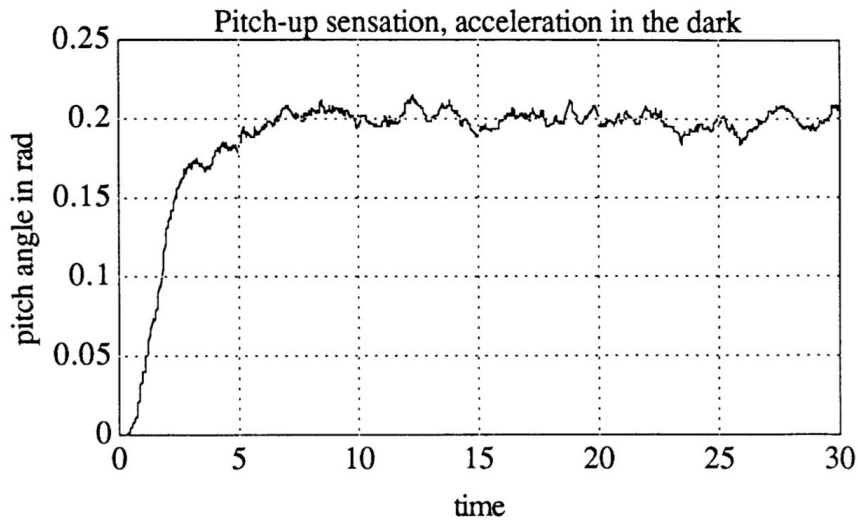
Figure 6: *Pommellet's orientation model response. Pitch sensation during a step linear acceleration of 0.2g maneuver. (i.e. Illusturation of Somatogravic Illusion) [13]*

2.1.2 Visual Inputs

For a pilot, scanning the flight instruments is one of the most accurate and robust ways of perceiving the motion, position and attitude of the aircraft during the course of a flight. Unlike the vestibular measurements, visual scanning measurements occur at "discrete" times.

The impact of visual inputs on pilot expectation has been partly modeled. Newman extended Merfeld's observer model by adding visual cues [21]. Both Newman's and Borah's model allow for visual cues as the information coming from outside visual references: however, neither makes use of a visual model that samples the flight instruments.

Kleinman et al. employed a continuous optimal scanning model in which the pilot monitors two flight instruments. Those instruments display the information corresponding to a single-axis control task (longitudinal position of a hovering VTOL

aircraft). However, their Optimal Control Model does not include a vestibular model and a discrete-time visual scan.

2.1.3 Knowledge of Aircraft Dynamics

"Model-based", by definition, describes an observer with an internal plant model [11]. A Model-Based Observer (MBO) can integrate both the plant dynamics and the sensory inputs, thus producing and propagating estimates of the pilot's state expectations. Observers, in control theory, include a real-time simulation of the plant dynamics given knowledge of its control inputs (Figure 7). This internal plant model of the system (in this case an internal plant model of an aircraft) is formed by training and learning through experiences [12,13].

The actual plant dynamics (label 1 in Fig. 7) and the observer's estimate of the state ($\mathbf{x_{est}}$) from the internal plant model (label 3 in Fig. 7) are generated in parallel. The discrepancy between measures of the actual plant state, labeled 2, and the observer estimations is called the residual (error), labeled 4. These residuals, weighted by an Observer Gain ($\mathbf{K}$), are eventually used to correct the state estimates. Pilot sensory inputs construct the measurement space in this case.
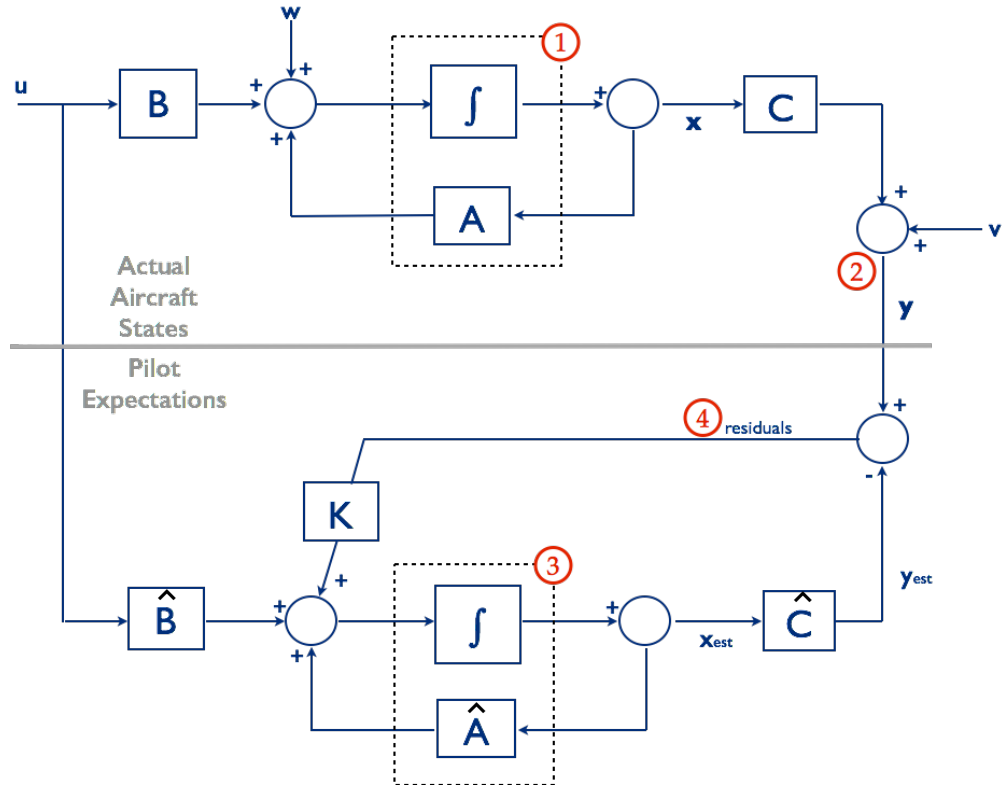
Figure 7: *Basic MBO structure*

This application of an MBO to model pilot's best possible expectation builds on an earlier work by Kleinman et al. who verified that the human manual control behavior characteristics of the human operator are near optimal [14]. Their Optimal Control Model (OCM) used several components to predict task performance in a manual-tracking task, including an MBO as well as a model of manual control. They applied the OCM to analyze the manual control of longitudinal position of a hovering VTOL aircraft and empirically verified that it predicted the outcome well [15]. According to Kleinman's studies, residuals weighted with the optimal Observer Gains would represent the pilot's best possible state expectations of the aircraft. However, Kleinman's work did not explicitly integrate different models of visual and vestibular sensing, and thus did not reach this thesis's ultimate objective of predicting mechanisms of potential SD.

2.2 The Vestibular System Models

Many models have been propsed of the vestibular system. Some studies focus only on the sensors themselves (SCC and otolith) and try to investigate the dynamics of relationship between motion and resulting afferent firing rates [30, 34-37]. Other studies integrate these sensory dynamics into a mutli-sensory model for orientation modeling purposes [18, 35, 13, 39, 38, 10].

Many of models of the SCC dynamics are based on mathematical models of a torsion-pendulum. This stems from Steinhausen's observation of the physiological mechanism underlying the SCC's measurement of angular acceleration and velocity: the deflection of the hair cells caused by the fluid motion in the SCC due to angular accelerations. In this sense, the internal fluid has an effective moment of inertia. Damping is caused by the viscous forces related to the flow of this fluid through the canals, and the spring-like structure of the hair cells cause a mechanical resistance in case of an angular motion.

In early attempts to find the proper parameters for this second-order SCC model, researchers relied on empirical data [50]. Young improved the simple torsion-pendulum model in 1968 with the augmentation of a new "adaptation" term that attempts to describe the SCC's decreased sensitivity to a continuing stimulus [19, 41]. In the mean time, there was no intensive research on modeling the otolith. Young proposed a simple first order equation with acceleration and jerk terms [19]. Thus, the SCC modeling efforts are considered to be quite accurate based on the empirical studies, while the otolith models are not as validated [13].

Fernandez & Goldberg studied both the SCC and the otolith extensively in 1971 and 1976, respectively [30, 37]. They conducted the most thorough study of the vestibular afferents firing rates in mammals. They ran a series of experiments using squirrel monkeys as subjects and proposed new mathematical models for both sensors. According to the frequency domain analysis conducted by Frenandez & Goldberg, the

behavior of the SCC was deviating from the torsion-pendulum model at both high and low frequencies. In other words, the previous SCC models were reliable only within a certain frequency range and within that range the measures are proportional to the angular velocity. Out of this frequency range, sensor readings are considered inaccurate.

This ambiguous behavior of the SCC sensors is mentioned in most of the related literature work. Here are two different quotes from two different fields of studies:

"Neural firing in the vestibular nerve is proportional to head velocity over the range of frequencies in which the head commonly moves (0.5-7 Hz). In engineering terms, the canals are 'rate sensors'."
Anatomy and Physiology of the Normal Vestibular System [40]

"At a frequency range between 0.1 and 5.0 Hz, which corresponds to that normally generated during natural movements such as locomotion, stepping, and jumping, the activity of the first-order afferent signals from the semicircular canals is close to being in phase with velocity (Melvill Jones & Milsum 1965)."
Spatial Orientation in Aviation [12]

Fernandez & Goldberg, in 1971, addressed this issue by adding two terms to the classic torsion-pendulum model: one for low, another for high frequency deviations. [37] Therefore, they represented the SCC dynamics in the following form:

$$H_{SCC}(s) = H_{TP}(s).H_A(s).H_L(s) \qquad \textit{Eq. 1}$$

where:

$$H_{TP}(s) = 1/[(1 + \tau_1 s)(1 + \tau_2 s)] \qquad \textit{Eq. 2}$$

(TF of torsion pendulum)

$$H_A(s) = \tau_A s/(1 + \tau_A s) \qquad \textit{Eq. 3}$$

(Phase lead at low frequencies, lead to gain attenuation at very low frequencies)

$$H_L(s) = (1 + \tau_L s) \qquad \textit{Eq. 4}$$

(Lead component and reproduces the high-frequency deviations from the torsion-pendulum model)

By merging the mathematical model of the torsion pendulum (H_{TP}) with the phase lead (H_A) and the lead component term (H_L) results in the transfer function below. The four time constants ($\tau_1, \tau_2, \tau_A, \tau_L$) are estimated based on experimental measurements gathered from squirrel monkeys. This defines the SCC afferent rate with respect to the angular acceleration stimulus.

$$\frac{SCC\ afferent}{Angular\ acceleration} = \frac{80s\ (1+0.049s)}{(1+80s)\ (1+5.7s)(1+0.0033s)} \qquad Eq.\ 5$$

At low frequencies, the discrepancy is mainly due to the phase lag. It is enhanced by addition of a phase lead component, which lead to gain attenuation at very low frequencies. At the end, they concluded by finding out a "reasonably good" agreement between the transfer and the experimental data in high and low frequency ranges (Figure 8).
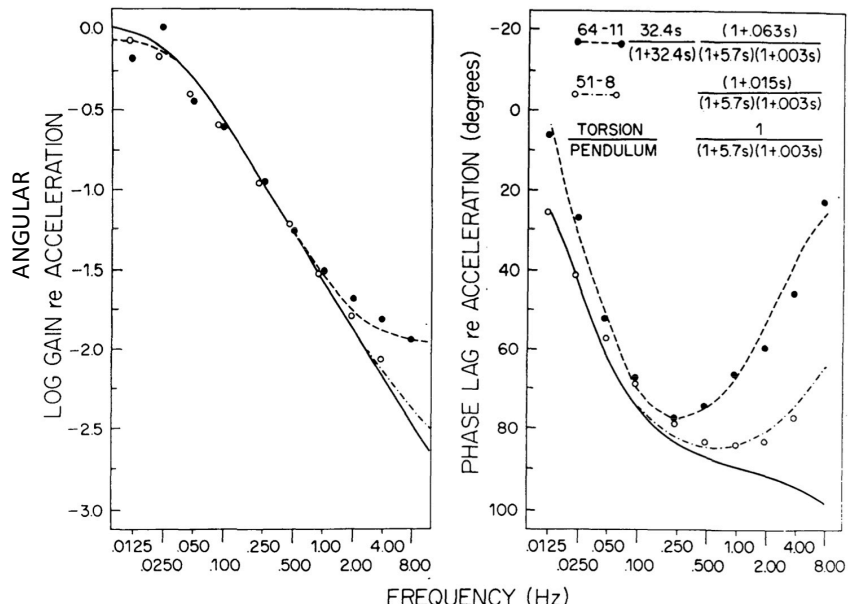
Figure 8: *High and Low Frequency deviations of the torsion pendulum from the experimental data, and the enhancement terms augmented to the torsion pendulum model [37]*

The SCC model developed by Fernandez & Goldberg is generally considered to be an accurate representation of the SCC sensor dynamics. Thus, many of the current studies are still based on this model. Ormsby, in 1974, developed and verified an SCC model using Fernandez & Goldberg's experimental results. For the SCC model, Ormsby proposed adding two terms to the torsion-pendulum model. One is for adaptation dynamics and the other one is for rate sensitivity, which is needed for abrupt changes in the angular velocity. In the same study, Ormsby proposed an otolith model as well. However, given the lack of definitive experimental data available at that time for otolith, the otolith sensor is modeled as a mass immersed in a fluid and restrained by the mechanical restraints such as viscous forces [36].

Merfeld modified and simplified the SCC model that has been deduced by Fernandez & Goldberg in 1971. Unlike Fernandez & Goldberg's SCC, which uses angular acceleration as the input, Merfeld's model uses angular velocity, and applies the SCC in a mutli-dimensional sensory conflict model. The otolith transfer function is approximated as unity. Merfeld's sensor dynamics are still being used in many of the mutli-sensory orientation modeling studies.

$$\frac{Afferent\ firing\ rate}{Angular\ velocity} = \frac{\tau_l\ \tau_a\ s^2}{(\tau_l\ s+1)\ (\tau_a\ s+1)} \qquad \textit{Eq. 6}$$

The SCC in Equation 6 is modeled by Merfeld as a 2nd order high-pass filters with a fluid-hair cell interaction time constant τ_l of 5.7 seconds and a neural adaptation time constant τ_a of 80 seconds.

Pommellet developed a sub-optimal orientation model, which is another mutli-sensory model that comprises the vestibular sensors, and used Merfled's SCC system dynamics [13, 35]. One of the time constants is slightly different in Pommellet's implementation, which can be considered as a further simplification:

$$\frac{Afferent\ firing\ rate}{Angular\ velocity} = \frac{80.6\ s^2}{(80s+1)\ (6s+1)} \qquad \text{Eq. 7}$$

For the otolith model:

$$\frac{Afferent\ firing\ rate}{Specific\ force} = \frac{1}{(s+100)\ (s+0.1)} \qquad \text{Eq. 8}$$

This SCC model that is considered to be thoroughly investigated and well accepted in the literature, while it is still not true for the otolith models [13, 36]. Thus, the otolith model developed by Grant and Best is a fairly recent model [17]. These models have proven to work coherently in previous multi-sensory models.

2.3 Current Orientation Models as an Application of the Vestibular Models and Need for a New Model

Vestibular system models can be integrated into bigger, multi-sensory models. Borah et al. developed a human spatial orientation model, in 1988, using a steady state Kalman Filter for their observer based model that applies body dynamics as the internal plant, and four sensory systems [18]. This included an SCC model that responds to angular accelerations based on Young, Ormbsy and Fernandez & Goldberg's modeling efforts, and is primarily a heavily damped torsion pendulum with adaptation and rate sensitivity dynamics [19, 36, 37]. Their otolith model used is based on Young & Meiry, and Fernandez & Goldberg's work, based on a mechanical accelerometer with some additional rate sensitivity [30-41].

Borah et al. models a "naïve passenger" that only comprise of internal simulation of body and sensor dynamics. The maneuvers that are experienced by this passenger were also limited to simple motions such as rotation in yaw-axis. They have included a visual model that is based on out-of-the-window visual references, and does not include any instrument scanning since there is no aircraft involved.

Pommellet improved Borah et al.'s model by implementing an Extended Kalman Filter to account for the non-linearities in the system dynamics (i.e., body dynamics). This added more maneuvering capabilities to the model. However, the internal plant dynamics used in Pommellet's observer based model is, again, the body and sensor dynamics. However, Pommellet criticized Borah et al.'s model for being "quite far away what is believed to be acceptable values for the time constants of the different (vestibular system) dynamics" [13]. Thus, more recent and accepted vestibular systems are implemented to Pommollet's model. As mentioned previously, this model referred to Merfeld's work for the SCC model [35], Grant & Best for the otolith model [17].

Newman et al. (2012 & 2014) developed a new orientation model, called Orientation Modeling System (OMS), which is an extension of Merfeld's observer based orientation model [10, 38]. Newman added visual sensory information to include better prediction of orientation, position, and linear velocity estimates. The vestibular sensor dynamics used in the OMS is Merfeld's vestibular models as the model is considered to be an extension of Merfeld's work. Newman et al.'s model is aiming to investigate the orientation perception of the pilot in the commercial aviation context. Although the aircraft dynamics are not included into their observer model, their model can investigate orientation expectation with the maneuvers that are known to potentially trigger SD.

As explained earlier, the MBO is part of the classic structure of the Optimal Control Model (OCM). The OCM is used to model and predict human manual control behavior, identify information requirements for manual control of aircraft, and develop flight control concepts such as stability augmentation [22]. The MBO, with the help of an optimal state estimator, produces aircraft state expectations optimally to reflect the "human operators *near optimal* response characteristics" [14].

However, the OCM focuses specifically on manual control performance and thus, included "neuromotor dynamics" to simulate the response-time lags and other muscular system dynamics to include the manual control aspect of the OCM. Since this thesis

limits the focus to cases of automated control (i.e. autopilot) with no manual control, there is no need to incorporate manual control characteristics.

None of these formerly developed models included an internal model of aircraft dynamics reflecting pilot expertise. If the mechanisms of SD are to be investigated, all of the major orientation perception contributors ought to be integrated. An expert pilot's knowledge of the aircraft dynamics, and sensory information should be integrated to have a better understanding of SD mechanisms. Therefore, a model of the pilot's best possible expectation of aircraft state needs to integrate sensory models (visual sampling model and vestibular model) with the pilot's internal aircraft model (knowledge of the system dynamics).

CHAPTER 3

OBJECTIVE 1: DEVELOPMENT OF THE MODEL

This thesis develops a novel computational model predicting the pilot's best possible expectation of the aircraft states by applying a Model-Based Observer (MBO) to integrate an internal model of pilot expertise with models of visual scanning and vestibular sensing. The model was developed in a C++ simulation framework called Work Models that Compute (WMC), which has been developed by the Georgia Institute of Technology Cognitive Engineering Center (CEC) [23]. This simulation provides a high fidelity, 6-Degree-of-Freedom Boeing 747 model as the representation of the 'true' aircraft dynamics.

The first major component described in this chapter is the MBO, which provides an "internal simulation" of the state estimates, and corrects these estimates with measurements of the aircraft states from the visual and vestibular models. This chapter begins with a discussion of the MBO, its structure, and how it can be used as a best-possible pilot expectation model. The other major components of the MBO are the two sensory system models, which are detailed in the second and third sections of this chapter.

3.1 Model-Based Observer

The best-possible pilot expectation applies an "internal simulation" of the aircraft dynamics. The estimated state within the MBO is propagated with the help of an accurate linear model of the aircraft dynamics, and is corrected continuously by the vestibular system and at discrete intervals by the visual sampling. To optimally combine both continuous-time and discrete-time measures, the MBO employs a Kalman Filter closer to a Hybrid Extended Kalman Filter design.

The state vector representation of the MBO **(States of Aircraft)** can be listed as:

- (X_1) Altitude
- (X_2, X_3, X_4) Linear Velocity
- (X_5, X_6, X_7) Angular Velocity
- $(X_8, X_9, X_{10}, X_{11})$ Attitude (Quaternion)

Unlike the multi-sensory orientation models described in Chapter 2 (Borah and Pommellet [13, 18]), these states only describe the aircraft dynamics without also containing any internal states of the vestibular system. In the MBO, non-linear dynamics of the sensory dynamics are linearized around the nominal state vector to generate the desired measurement matrix, **C**.

Figure 9 details the structure of the MBO. The observer state vector (**x**) contains the variables of the aircraft state needed to assess the pilot's expectation of the motion as shown above.
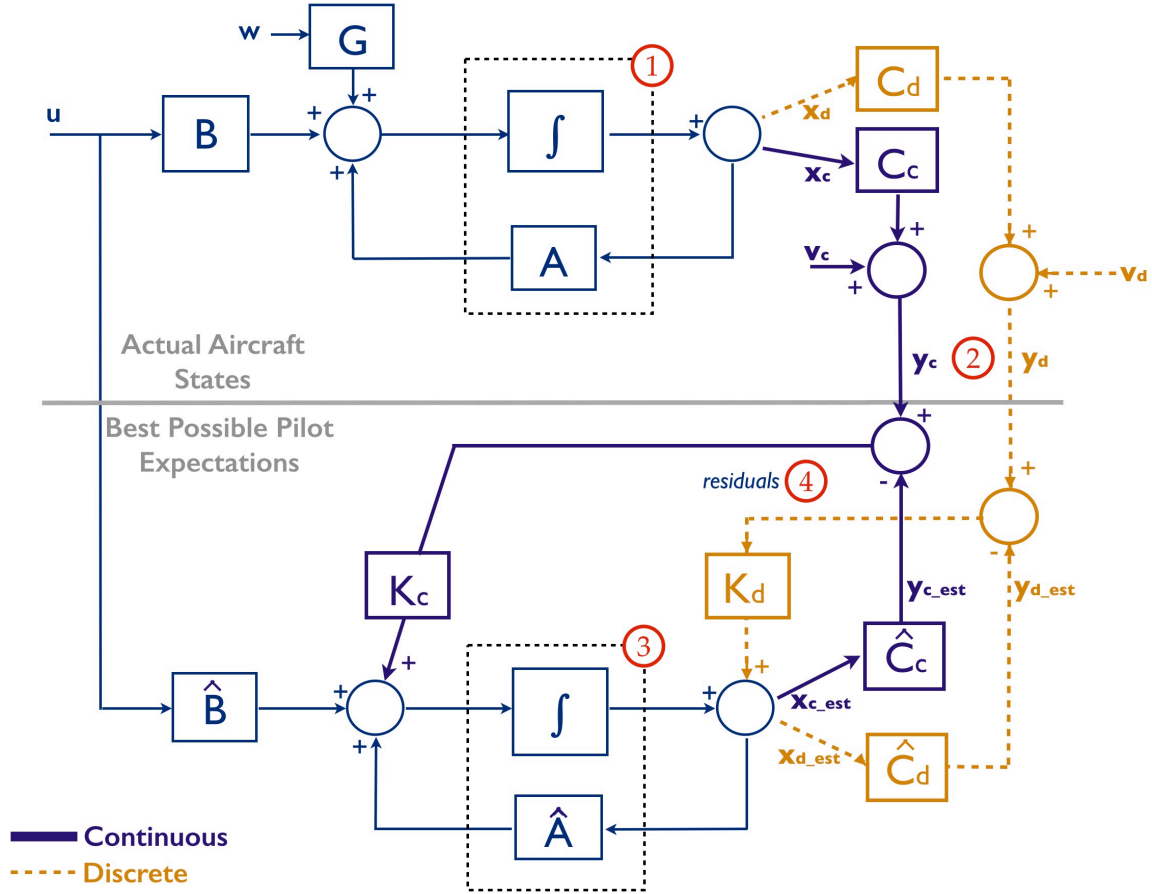
Figure 9: *The MBO - Model of Aircraft Dynamics and Pilot's Best Possible Expectations*

The MBO is tightly coupled to the aircraft simulation that describes the dynamics of the system. The straight signal paths illustrate continuous-time signals while the dashed lines illustrate discrete-time signals. The MBO assumes a model of the aircraft dynamics as shown in label (1) propagates the aircraft state vector (**x**) with additive process noise (**w**), weighted by (**G**), that has zero mean and a covariance of (**Q**). The measured or observed state variables, label (2), account for the measurement errors (**v**). The continuous path carries the continuous signals coming from the vestibular system measurements (**y$_c$**). In the continuous case, measurement error is the vestibular sensors error denoted by (**v$_c$**). The discrete path carries the discrete signals due to the discrete visual measurements (**y$_d$**). In the discrete case, measurement error comprises the errors due to aircraft's sensor error, errors due to the design of the flight instrument, and errors

due to pilot's perception of the scanned instrument. Further discussion on measurement errors can be found in the next chapter (*Chapter 4: Parameterization and Verification/Validation*). Label (3) is the "internal simulation" of the aircraft dynamics maintained by the pilot ($\mathbf{x_{est}}$) as simulated with a linearized model of the aircraft. The measurement values that would be expected from $\mathbf{x_{est}}$, indicated as $\mathbf{y_{est}}$, are compared with the actual measurements $\mathbf{y}$, and the discrepancy, shown in label (4), is weighted by the Observer gain to correct $\mathbf{x_{est}}$.

To initialize the filter, the initial state estimates ($\mathbf{x_{est,0}}$) are set equal to the actual aircraft state. This assumption also sets the initial value of the error-covariance ($\mathbf{P_0}$) be zero.

The error-covariance is defined as Eq. 9:

$$P \;=\; E[(x(t)- \hat{x}(t))(x(t)- \hat{x}(t))^{T}]$$

Eq. 9

$\mathbf{P}$ is propagated by integrating the continuous Algebraic Riccati Equation (ARE) through time (Eq. 10). The continuous ARE assumes the continuous vestibular inputs are weighted by the Kalman gain $\mathbf{K_c}$. In case of a discrete measurement, $\mathbf{P}$ is updated by using the discrete ARE equation with the Kalman gain $\mathbf{K_d}$ (Eq. 11).

$$\dot{P} \;=\; AP + PA^{T} + GQG^{T} - P\,C_c^{T}R_c^{-1}C_c\,P$$

Eq. 10

$$P^{+} \;=\; (I - K_{d_k}C_{d_k})\,P^{-}\,(I - K_{d_k}C_{d_k})^{T} + K_{d_k}R_{d_k}K_{d_k}^{T}$$

Eq. 11

The Kalman gains for both continuous-time and discrete-time (K_c & K_d) are set to minimize the trace of $\mathbf{P}$, i.e. minimize the discrepancy between $\mathbf{x_{est}}$ and $\mathbf{x}$ as given in Eqs. 12.

$$K_{d_k} \;=\; P^{-}\,C_{d_k}^{T}\,(C_{d_k}\,P^{-}\,C_{d_k}{}^{T} + R_{d_k})^{-1}$$

$$K_c \;=\; P^{-}\,C_c^{T}\,(R_c)^{-1}$$

Eq. 12

The pilot's best-possible expectation of the aircraft state, $\mathbf{x_{est}}$, is propagated using Eq. 13:

$$\dot{\hat{x}} = A\hat{x} + Bu + K_c (y_c - C_c \hat{x})$$

Eq. 13

Discrete visual measures are used to correct $\mathbf{x_{est}}$ using Eq. 14:

$$\hat{x}^+ = \hat{x}^- + K_{d_k} (y_d - C_{d_k} \hat{x})$$

Eq. 14

To correct the internal expectations of the aircraft state, the visual and vestibular cues (i.e. the measurements) feed information to the MBO through the measurement matrix ($\mathbf{C}$). The characteristics of these sensory measurements, and the generation of the measurement matrices are discussed in the next two sub-sections.

3.2 Visual Sampling Model

The visual sampling model focuses only on flight instrument scanning, and provides the discrete measures ($\mathbf{y_d}$). Pilot visual sampling is simulated by a "scan-action" structure that may be applied to many different scanning patterns. In the context of this thesis, a scan-action defines the information gathered from flight instruments. For instance, the Altimeter scan-action provides altitude information, and the Airspeed scan-action provides information about airspeed. Table 1 relates flight instruments to their corresponding elements of the aircraft state.

Table 1: *Primary relations between the sensors and the state variables*

x	AI	ASI	Altimeter	HI	VSI	T/C	SCC	Otolith
h			✔					
u		✔						$\frac{d}{dt}$
v						✔(β)		$\frac{d}{dt}$
w					✔			$\frac{d}{dt}$
p							✔	
q							✔	
r						✔	✔	
θ	✔							✔
ϕ	✔					✔		✔
ψ				✔				

—————— Basic-T ——————   —— Vestibular ——
—————————— Basic-Six ——————————

To investigate various scan patterns, there is one scan-action for each of the scanned flight instruments. A flight scenario with a "basic-T scan" scans the Attitude Indicator, Airspeed Indicator, Altimeter, and Heading Indicator, and thus involves 4 scan-actions.

Each scan-action includes the binary measurement matrix (**C**) that relates aircraft states into the measurement to be made. For visual sampling measurements, set by the scan-actions, the visual measurement matrix (**C$_d$**) is a straightforward binary matrix that consists only of 0s and 1s. This is because the visual sampling model simply measures the state elements via flight instruments.

For instance, the *altitude scan-action* measures only the altitude state of the aircraft. Thus, the corresponding measurement matrix, for the altimeter scanning, would

have 1 for the altitude state and 0's for the rest of the state elements. Since, the altimeter scanning only measures one component, the altitude value (h), the visual measurement matrix, for this particular scan-action, is a 1-by-N matrix, where 1 corresponds to the number of measured states, and N is the total number of aircraft states used in the MBO (N = 11).

The visual measurement matrices used in the MBO for the four Basic-T instruments are listed below.

Altimeter (h)

$$C_h = [\ 1 \quad 0 \quad 0 \quad 0 \quad 0 \quad \cdots \quad \cdots \quad 0\ ]$$

Airspeed Indicator (V)

$$C_V = \begin{bmatrix} 0 & u/V & 0 & 0 & \cdots & \cdots & \cdots & 0 \\ 0 & 0 & v/V & 0 & 0 & \cdots & \cdots & 0 \\ 0 & 0 & 0 & w/V & 0 & 0 & \cdots & 0 \end{bmatrix}$$

Since the total airspeed (V) has a non-linear relationship with its components (i.e., $V^2 = \sqrt{u^2 + v^2 + w^2}$), the airspeed scan-action provides a measurement matrix that is solved for at each time step.

Attitude Indicator and Heading Indicator ($\theta, \phi, \& \psi$)

$$C_{ATT\&HEAD} = \begin{bmatrix} 0 & \cdots & 0 & 0 & 1 & 0 & 0 & 0 \\ 0 & \cdots & \cdots & 0 & 0 & 1 & 0 & 0 \\ 0 & \cdots & \cdots & \cdots & 0 & 0 & 1 & 0 \\ 0 & 0 & \cdots & \cdots & \cdots & 0 & 0 & 1 \end{bmatrix}$$

The state vector used in the MBO includes attitude quaternions to define the orientation of the aircraft. Both attitude and heading indicators provide information about the attitude of the aircraft. Therefore, these scan-action triggers a discrete update of the

attitude quaternion states. Since quaternion is a four-element vector, the measurement matrices for the attitude and heading indicator are 4-by-N matrices.

The scan-action, then, adds randomly generated zero mean, white-noise error with covariance **R**:

$$v \sim N(0, \ R)$$

This generic visual sampling model can then be applied to create discrete measures of any state or set of states variables at times representing a range of scanning strategies, including periodic scans at specified frequencies or episodic scans triggered by events. These provide asynchronous "discrete" visual observations to the MBO.

3.3 Vestibular Model

The SCC model used in this thesis is based on Merfeld's work (Eq. 15) [35]. For the otolith model, similar to Pommellet's orientation model, Grant & Best's otolith model is applied (Eq.16) [18]. These models express the sensor dynamics in transfer function form.

$$SCC(s) = \frac{(80) \ (5.7) \ s^2}{(80s+1) \ (5.7s+1)} \qquad \textit{Eq. 15}$$

$$OTO(s) = \frac{1}{(s+100) \ (s+0.1)} \qquad \textit{Eq. 16}$$

An important aspect of the vestibular system is the sensor threshold. For motions beyond this threshold, the SCC model takes the angular acceleration components as input to its transfer function and outputs angular velocity. Likewise, for motions above its threshold, the otolith provides Gravito-Inertial Forces (GIFs) continuously, given linear acceleration and orientation. In the case of a sub-threshold maneuver, the vestibular system outputs provide zero measurement. In other words, the pilot is assumed to be

29

getting zero angular velocity measurements from his/her SCC.

As mentioned earlier in the *Chapter 2: Background*, the MBO implements the threshold values defined by Mulder's Law for the SCC measurement. All three axes threshold values are defined as 2.5 deg/s according to Mulder's Law [31]. The otolith thresholds considered for the MBO are defined as 0.06 m/s^2 by Guedry's empirical studies. However, the otolith thresholds are fairly small and do not contribute to the somatogravic illusions [12]. Thus, the current MBO does not apply an otolith threshold.

A continuous measurement-provider-action is constructed for both SCC and otolith with a similar structure to the scan-actions constructed for the visual sampling model and provides the (**C**), and (**v**) corresponding to the measurement. However, to include the dynamics of the vestibular system, the vestibular measurements reflect the state of the vestibular models given in equations 15 & 16, and then measurement error is introduced randomly. The sensor error (equivalent to measurement error in the vestibular case) (**v**) associated with vestibular system can be found in the Borah & Young et al.'s model [18]. Their sigma sensor error values for the SCC are defined as: $\sigma_x = 0.01$, $\sigma_y = 0.01$, $\sigma_z = 0.0316$. The otolith sigma sensor error values are equal to each other and are $\sigma_{x,y,z} = 0.0316$.

Contrary to the visual sampling model, the vestibular model measurements have internal dynamics (Eq. 15 & 16), and thus, the vestibular model's measurement matrix (**C$_c$**) must be generated through linearization, shown in Eq. 17.

$$C_c = \left.\frac{\partial y}{\partial x}\right|_{x_n} \qquad\qquad \textbf{\textit{Eq. 17}}$$

The continuous measurement matrix for both the SCC (**C$_{SCC}$**) and the otolith (**C$_{OTO}$**) are generated through linearization of the internal sensor dynamics. In this sense, "**y**", in the Eq. 17, represents the output of the vestibular system. The "**x**" indicates the state vector of the aircraft. The linearization process, basically, perturbs the state

elements of the system (the aircraft) to see the perturbations' effects on the sensor output, and thus, generates the continuous vestibular measurement matrices ($\mathbf{C_c}$).

3.4 Software Implementation

The MBO consists of 2 different software sections: the continuous-MBO provided with the continuous inputs from the vestibular model, and the discrete-MBO provided with visual scans at discrete times. These two sections are integrated via the *model integration schema* shown in Figure 10. The upper portion of the Figure 10 shows the measurement actions: discretely triggered scan-actions (visual sampling model) in the upper right corner (scan airspeed, scan altitude, etc.) and continuous vestibular measurements in the upper left corner. Vestibular measurements (SCC and otolith) are fed into the continuous-MBO continuously while visual measurements trigger updates in the discrete-MBO. Both act upon the same variables $\mathbf{x_{est}}$ and $\mathbf{P}$: the continuous-MBO sets $\mathbf{x_{est}}$ and $\mathbf{P}$ continuously, and the discrete-MBO gets and corrects them at the discrete times when there is a discrete visual measurement.
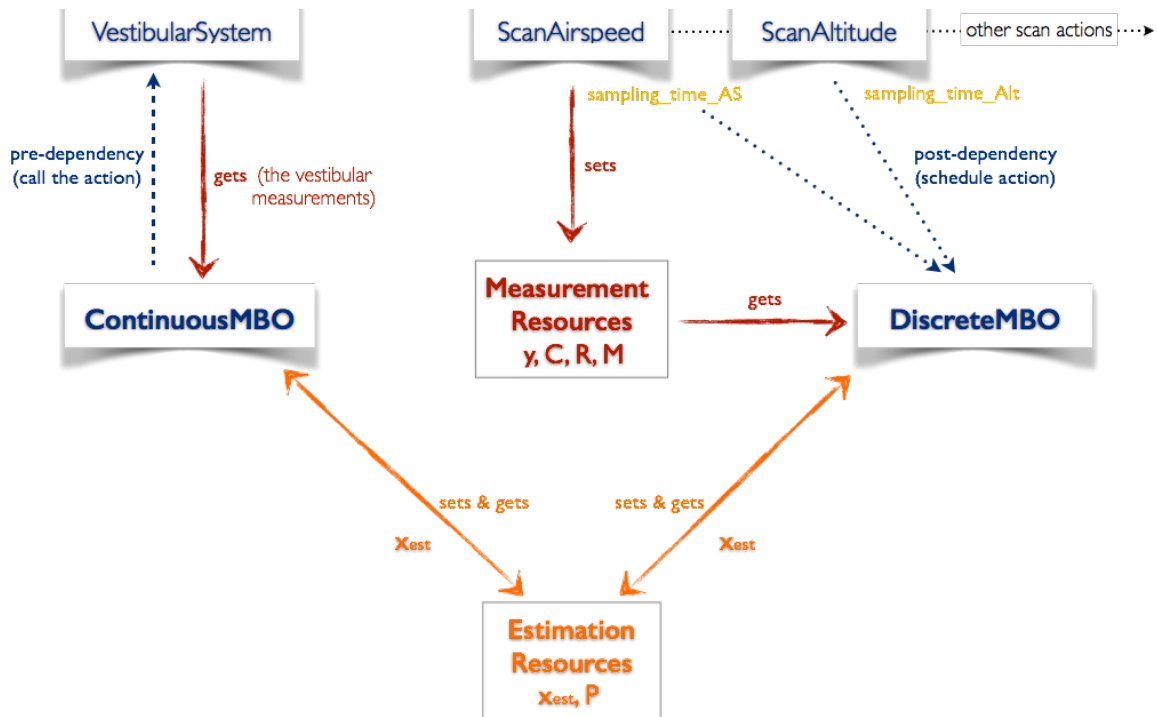
Figure 10: *MBO, Model integration schema*

3.4.1 Visual Scan-Actions

As it can be seen from the upper right portion of the Fig. 10, there is one scan-action for each of the flight instruments. This allows the analyst to discretely schedule them either synchronously or asynchronously at the desired frequencies by setting "sampling times". Having this discretely-triggered visual sampling model structure makes it possible to implement wide variety of scan behaviors or patterns to reflect both nominal and off-nominal cases:

- *T-Scan* scan behavior is considered to be a baseline/benchmark pattern that exhibits an optimal instrument sampling. In this configuration, the pilot is assumed to be scanning all of the necessary instruments at a high enough frequency to have reasonable expectations of the states.

- *The Distraction* scan behavior is defined as ceasing to sample one or a set of flight instruments for the duration of a desired time interval. Thus, specific

instruments are omitted by not scheduling them during the desired distraction time intervals.

- *The Emphasis* scan behavior reflects the cases where one or a set of instruments is scanned more frequently compared to the rest of the instruments, by setting two different sampling time values: one for high frequency, and one for low frequency scanning.

Several variations of scan behaviors can be developed since the scan-actions employ a generic and flexible structure. Each scan-action, at the end of its execution, sets the relevant measurement matrix and sensor errors for a particular flight instrument and feed them to the relevant MBO action (discrete-MBO) through a *measurement resource*, which comprises:

- **y**: measured state(s)
- **C**: measurement matrix
- **R**: sensor error covariance for the measured state(s)
- **M**: number of state(s) measured

Once scan-actions have been executed, they trigger the discrete-MBO in order to propagate the next state of the pilot's best possible expectations and the error covariance ($\mathbf{x_{est}}, \mathbf{P}$).

3.4.2 Vestibular Action

There is one action that provides the continuous measurements of the vestibular system. The information passed from vestibular action to the continuous-MBO is in the same form with the *measurement resource* listed above for the visual scan-action (**y, C, R, M**).

Since the actual vestibular sensory system continuously feeds sensory information to the Central Nervous System, the vestibular action, unlike discretely triggered visual

scan-actions, is scheduled at every time-step. Thus, the continuous-MBO continuously incorporate "vestibular measurement resources" in its propagation of pilot's best possible expectation of aircraft state, and the error covariance (x_{est}, P).

3.4.3 Linkage Between the Continuous-MBO and the Discrete-MBO

To capture the effects of both discrete visual sampling and the continuous vestibular system on the pilot's best possible expectation, the discretely and the continuously generated expectations have to be optimally combined.

Thus, the *estimation resource* stores the parameters required to link the discrete-MBO to the continuous-MBO:

- x_{est}: Best possible expectation of the aircraft states
- P: Estimation error covariance

Whenever an MBO action (either discrete-MBO or continuous-MBO) needs to update, it gets the current x_{est} and P values from the *estimation resources* and updates x_{est} and P. Having this resource structure avoids the conflicts that may arise due to simultaneous measurement updates, and provides an organized flow of MBO resources.

CHAPTER 4

OBJECTIVE 2: PARAMETERIZATION AND VERIFICATION/VALIDATION

The first section of this chapter, Parameterization of the Model, discusses the error models that have been implemented and their parameterization process to ensure accurate model estimates. An estimation problem would be deterministic without the presence of random disturbance and/or noise in the system. For realistic results, the stochastic characteristics of both process error (due to external aircraft disturbances) and measurement error have been parameterized using previously developed error models.

The second section, Verification and Validation of the Model, begins with discussion of the process used to verify and validate the individual components. This section concludes with the validation of the overall model. The validation of the proposed model is mainly done using previously studied scenarios and former orientation models to confirm that the MBO predicts known illusions and concerns with spatial disorientation.

4.1 Parameterization of the Model

As the model complexity increases, model's sensitivity to error values also increases. Newman et al. criticize the stable Extended Kalman Filter implementations of human orientation perception models by Kynor and Selva for being highly dependent on model parameter assumptions [10, 51, 52].

"Results were also highly dependent on model parameter assumptions and sensitive to small deviations in the assumed sensor bandwidths or noise covariance matrices."

Newman et al. 2012 [10].

Thus, the MBO needs for process and measurement errors to be parameterized for accurate predictions, and for avoidance of instability and/or divergence of the Kalman

Filter estimations. Divergence, in the MBO, usually occurs due to singularities in the system. Changing aircraft dynamics (i.e., different flight regimes, various turbulence intensities, etc.), and using different sensors (i.e., various sensor dynamics) all requires re-tuning the model parameters. The following sub-sections will discuss (1) the process error parameterization, and (2) measurement error parameterization.

4.1.1 Modeling Process Error

The process error, in context of this thesis, is considered to be the external gusts experienced by the aircraft. It is denoted as (**w**) and the location of injection of this process was shown earlier in Figure 9. Accurate knowledge of the process error covariance (**Q**) is crucial to a Kalman Filter.

When used off-line for the analysis purposes, there are multiple approaches for modeling wind gust/turbulence for simulation purposes, the most popular of which are based on stochastic methods. Two of the most common stochastic models are the von Karman and the Dryden model [24, 43]. The Dryden model has been adopted in this thesis.

The Dryden model is based on empirically measured power spectra of wind velocity in turbulent air and it assumes gusts to be random, homogenous and isotropic [44]. The power spectral density of the gusts is determined based on turbulence field properties, such as the turbulence scale length and turbulence intensity (RMS gust velocity) [45]. The Dryden transfer functions are, then, derived from those power spectral densities by performing a process called "spectral factorization". The transfer functions are used as shaping filters to generate the gust velocity components from Gaussian white noise. Gust velocity components include both linear (u, v, w) and angular (p, q, r) attributes of the turbulence [46].

To apply the Dryden model to the 6-Degree-of-Freedom aircraft model, the appropriate turbulence scale length and turbulence intensity should be set to describe the

turbulence level experienced by the aircraft in any particular simulation run. The desired attributes of the turbulence and the shaping filter transfer functions can be found by referring to previously developed Dryden models.

In this project, the medium/high altitude (>2000 feet) Military Specification MIL-8785C is implemented [47]. All six gust velocity transfer functions and turbulence attributes are specified below in Table 2 and in Figure 11, respectively. The scale length of the turbulence is equal to 1750 feet for all three components (i.e. $\mathbf{L_u}$, $\mathbf{L_v}$, $\mathbf{L_w}$) at altitudes 2000 feet and above. The turbulence intensities (i.e. $\boldsymbol{\sigma_u}$, $\boldsymbol{\sigma_v}$, $\boldsymbol{\sigma_w}$) can be determined from Figure 11, based on the altitude and the probability of the turbulence intensity being exceeded. All three components of the turbulence intensity are assumed to be equal to each other.

Table 2: *Medium/High Altitude MIL-8785C Dryden Model [Ref. MIL-8785]*

$$H_u(s) = \sigma_u \sqrt{\frac{2L_u}{\pi V}} \frac{1}{1+\frac{L_u}{V}s}$$

$$H_p(s) = \sigma_w \sqrt{\frac{0.8}{V}} \frac{\left(\frac{\pi}{4b}\right)^{1/6}}{L_w^{1/3}\left(1+\left(\frac{4b}{\pi V}\right)s\right)}$$

$$H_v(s) = \sigma_v \sqrt{\frac{2L_v}{\pi V}} \frac{1+\frac{\sqrt{3}\,L_v}{V}s}{\left(1+\frac{L_v}{V}s\right)^2}$$

$$H_q(s) = \frac{\mp\frac{s}{V}}{\left(1+\left(\frac{3b}{\pi V}\right)s\right)} \cdot H_v(s)$$

$$H_w(s) = \sigma_w \sqrt{\frac{2L_w}{\pi V}} \frac{1+\frac{\sqrt{3}\,L_w}{V}s}{\left(1+\frac{L_w}{V}s\right)^2}$$

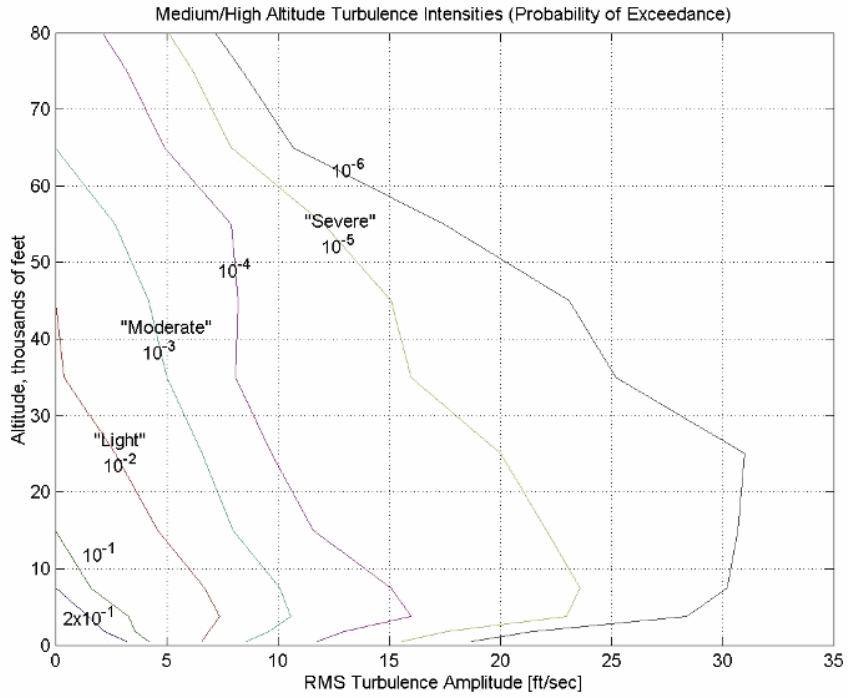$$H_r(s) = \frac{\mp\frac{s}{V}}{\left(1+\left(\frac{4b}{\pi V}\right)s\right)} \cdot H_w(s)$$

Figure 11: *Turbulence intensity (RMS Amplitude) vs. Altitude [47, 48]*
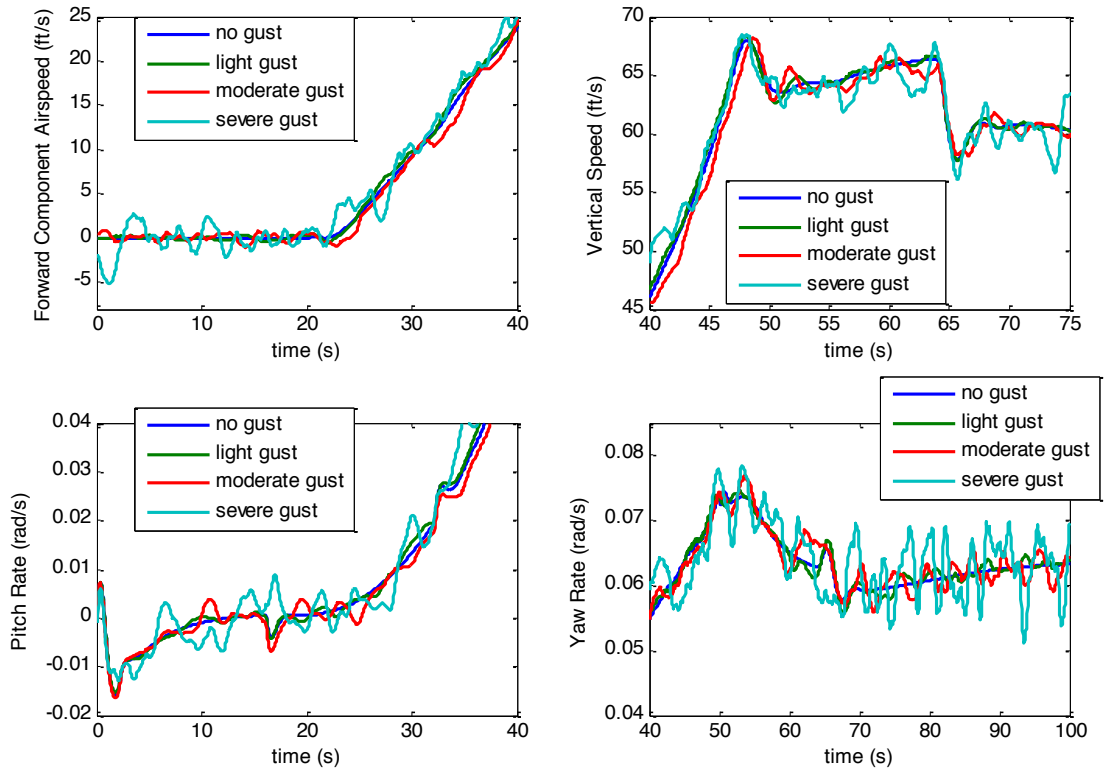

Figure 12: *Airspeed and angular velocity components with various turbulence intensities*

To illustrate the impact of the gusts, Figure 12 shows the effect of various turbulence intensities on relevant of the aircraft states.

Introducing the best process error values to represent the white noise component of the gusts help to overcome the issues caused by the modeling mismatches [26]. Especially, since the Dryden gust model does not introduce an uncorrelated pure, white noise to the aircraft dynamics, there is a need for some process error to best represent the aircrafts dynamics with gusts [47, 49].

The process error ranges have been found by trial and error method for various turbulence intensities (light, moderate, and severe turbulence). These ranges are determined by ensuring that the process error values selected satisfy the Kalman Filter operation and stay within the 2-sigma bounds. For most of the process error values that lay outside of this determined range, the Kalman Filter estimates diverge.

Table 3: The process error ranges found for each of the states

	No or light turbulence	Moderate Turbulence	Severe Turbulence
Altitude [ft]	100	250	500
Linear Velocities (for x, y, z) [ft/s]	35 5 10	200 60 75	400 10 150
Angular Velocities (for x, y, z) [rad/s]	0.04 0.04 0.04	0.1 0.1 0.1	0.2 0.2 0.2
Quaternions	0.04	0.08	0.13

4.1.2 Measurement Error

Measurement error, denoted as (**v**) previously, is also modeled as Gaussian white noise. Figure 9 indicates the location of the injection of the measurement error both for the continuous and the discrete measurements.

Measurement error (**v**), for the visual measurements, includes not only the noise in aircraft's sensors: flight instrument design can also highly influence the perceived measurement. For example, an altimeter with a thick needle can contribute adversely to the measurement error by causing an increase in its variance. Thus, measurement error here represents the error in the pilot's expectation of the aircraft states from all causes.

For vestibular system error, measurement error is considered only to be the vestibular sensory error. A number of studies exist have examined the uncertainties in pilot expectation. Curry et al. studied the effects of signal-to-noise ratio on the vestibular-only system [25]. They found that a representative noise to signal ratio for vestibular measurements is approximately -18dB. Alternatively, Borah et al.'s optimal estimator for human spatial orientation design uses an empirically driven error model [18], in which experimental data is used to parameterize error values as error-covariance matrices. These error models are utilized as an initial point for the parameterization of the model. All these parameters can be used as an initial point for this MBO's parameterization.

Borah et al., in their paper, discuss how they "tuned" their measurement errors to bring the model responses closer to the empirical human-in-the-loop experiment results [18]. Since the measurement errors are unknown and impossible to measure, it gives the modeler flexibility as long as the model responses are within a reasonable range. That's why the term "tuning" makes sense when it comes to model parameterization.

Here, the parameterization explores the range of measurement errors that the MBO For this purpose, measurement error value ranges are found both for the visual measurements and for the vestibular measurement.

Table 4: *The measurement error values for the discrete visual measurements*

	Lower Bound	Nominal	Upper Bound
Altitude [ft]	1	50	100
Linear Velocities [ft/s]	0.05	10	150
Angular Velocities [rad/s]	0.002	0.015	0.4
Quaternions	0.001	0.015	0.04*

The sigma error values for the continuous vestibular measurements used in the MBO are parameterized based on the previously developed models [18]. The MBO's stability and accurate representation of the vestibular model responses were the criteria for this parameterization process. The measurement sigma error values used for the SCC are $\sigma_x = 0.035$, $\sigma_y = 0.041$, $\sigma_z = 0.043$. For the otolith, all three components' errors are defined as $\sigma_{x,y,z} = 3.16e\text{-}3$.

For the most part, these error ranges were found by using the same trial and error method as disused earlier in sub-section *4.1.1 Modeling Process Error*. The primary criterion during this procedure was avoiding the singularities. The nominal measurement error values are used for many of the experiments ran for validation/verification purposes. These values reflect reasonable error values for each of the states. These lower and upper bounds indicate a range of measurement error values that can be used with the MBO, and exhibits accurate representation of expectation. The asterisk (*) defines a hard bound for quaternions, meaning there will be a singularity issues in case a higher error value. So, most of the measurement error values that lay outside of these hard bounds caused singularity in the system, thus divergence in the KF estimations.

4.2 Verification of the Model Components

The following sub-sections explain the verification process of each of the individual model components. First, the MBO itself is verified to produce estimates that are within their predicted statistical bounds. Then, the vestibular system implementation, the semi-circular canal (SCC) model, and the otolith model are verified. The Dryden gust model verification concludes the discussion of *The Verification of the Model Components* section.

4.2.1 The Kalman Filter

To verify that the implemented Kalman filter, the core of MBO, is working properly, the error propagation matrix (**P**) can be observed. Since Gaussian error models provide input to the MBO, estimation errors (**x-x_est**), i.e., the discrepancy between the pilot's best possible expectation and the actual state of the aircraft, are also expected to have a Gaussian distribution. Therefore, in a properly working Kalman filter, this estimation error should lie 95.4% of the time within the (-2σ) and (2σ) bounds predicted by the error covariance (**P**) [26] The 2-sigma bounds of every state is examined for all runs to make sure that the filter is tuned properly and providing accurate estimations of the aircraft states.

The estimation error ($x - \hat{x}$) can also be investigated to see if the distribution is similar to a Gaussian distribution. Figure 13 shows the normality test that was conducted for the pitch rate estimation error (q), as an example. It can be seen from the figure that the error has a distribution close to a Gaussian, and it has a p-value of 0.0184, based on a significance level of about 5%. Additionally, the predicted estimate error variance from the error covariance matrix (**P**) and the actual estimation error can be compared. For this particular case shown in Figure 13, the predicted variance is 9.12e-5 and the actual variance is 7.60e-5, i.e., the square of standard deviation 0.0087.
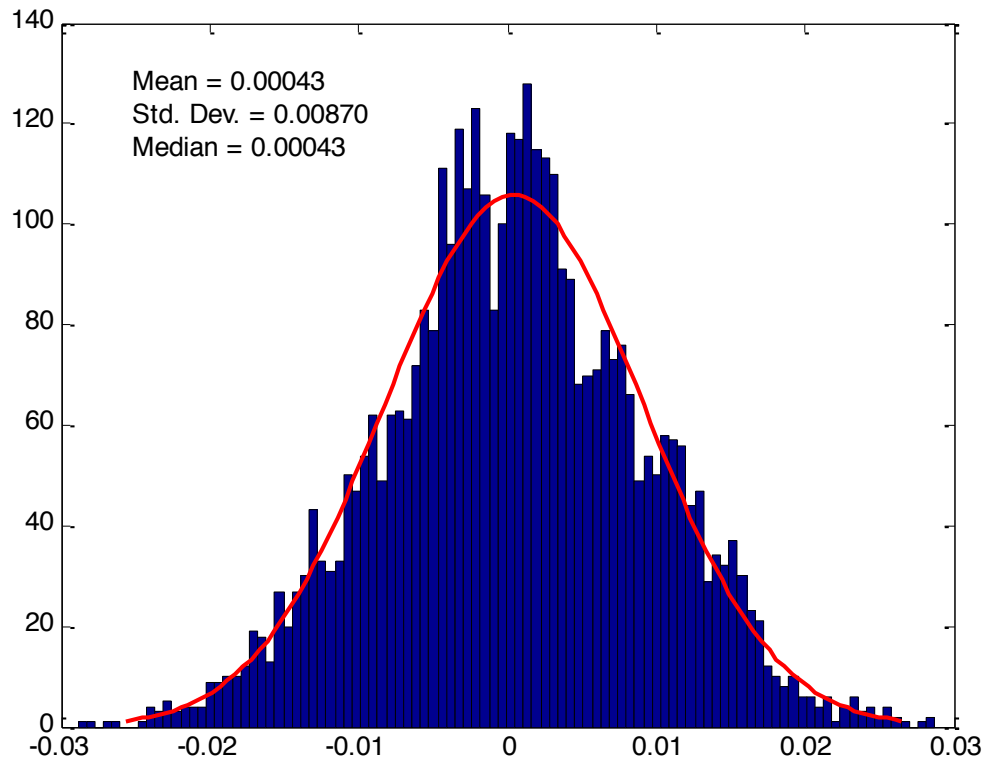
Figure 13: *Distribution of the estimation error values of the pitch rate (q)*

Figure 14 illustrates 2-sigma bounds and actual estimation errors of the airspeed for two different simulation runs. The blue lines construct the 2-sigma bounds for a particular simulation run, upper bound being the $+2\sigma$ value and lower being the -2σ value. The red line in between the 2-sigma bounds is the estimation error.
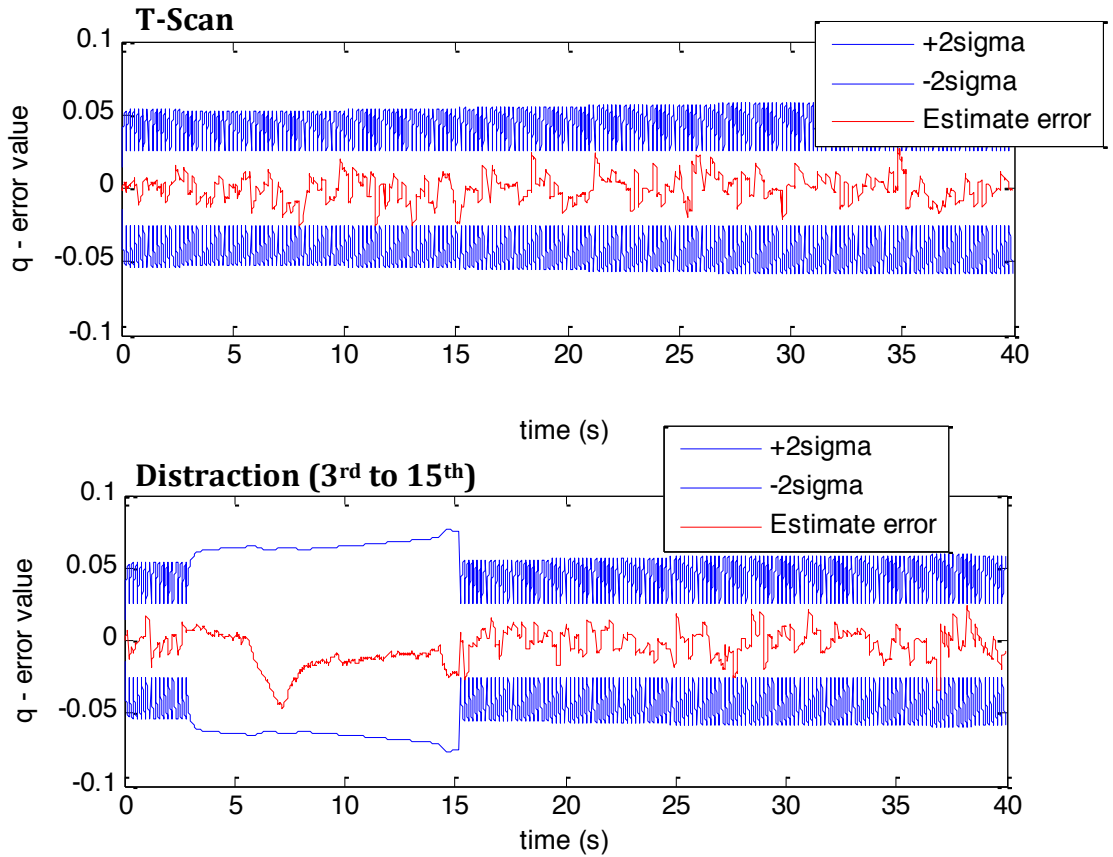
Figure 14: *2-sigma Error Bounds and Error in the pilot's expectation of the pitch component of the angular velocity and corresponding 95% confidence interval, during an above-threshold pitch-up maneuver executed at 5th second, with a high frequency visual scan (T-Scan) of all flight instruments and with a 18 seconds of distraction.*

The first plot in Figure 14 corresponds to a 'T-Scan' scan behavior, and thus expected to exhibit a benchmark with a low expectation error allowance (confidence interval). The bottom graph in the same figure corresponds to a 'distraction' scan behavior for 18 seconds starting at the time 3rd second. As anticipated, the pilot's error allowance (confidence interval) grows right after distraction starts. As soon as the pilot scans the relevant flight instrument (i.e. end of distraction) error allowance of the pilot goes back to its nominal value. All of the maneuvers, in this case, are performed above the vestibular threshold (i.e. above-threshold maneuvers), and thus both the visual scan and the vestibular sensors correct the pilot's expectation of aircraft state.
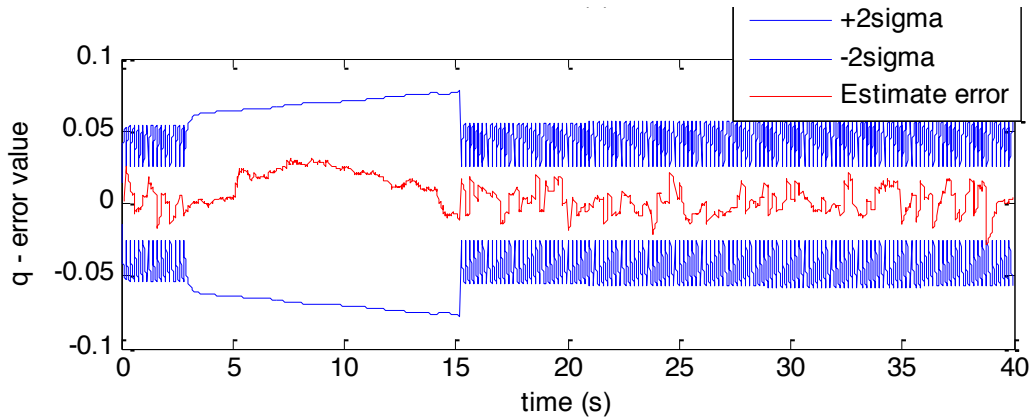
Figure 15: *2-sigma Error Bounds and Error in the pilot's expectation of the pitch component of angular velocity and corresponding 95% confidence interval, during a sub-threshold banking maneuver, with a distraction at the beginning of the maneuver (from 3rd second to 15th second).*

Figure 15 illustrates 2-sigma boundaries and estimation errors with a similar pitch-up maneuver as seen in Figure 14. However, the Figure 15 maneuver is performed below the vestibular threshold (i.e., sub-threshold maneuver), to see the effects of the continuous vestibular measurement on the 2-sigma bounds. In this particular case, the pitch maneuver starts at the 5th second, right after the pilot stops scanning the instruments and distraction goes on until 15th second. Since this is a sub-threshold maneuver, the pilot's vestibular system is not triggered and feeds continuous measurements of zero to the MBO for the angular velocity states of the aircraft. Therefore, compared to the bottom graph of Figure 14, the 2-sigma error bounds expand more due to absence of continuous vestibular measurements. For this model, as long as the process error and measurement error have covariance that are within the allowable range of the MBO, all of the 2-sigma graphs verify the Kalman Filter in the MBO is operating properly.

45

4.2.2 The Semi-Circular Canal Model

The vestibular system models implemented into the MBO are based on previously developed models. In this verification of the SCC, the implemented SCC model outputs are verified to make sure that the implementation is correct.

To verify the SCC model, its sensor outputs are compared with other model responses that have been validated by empirical results. Figure 16 compares the SCC output in a simple test case run to same stimulus in the Figure 17. This test case verification scenario is created in Matlab to see if the implemented model is able to reproduce the Borah et al.'s empirically driven model outputs. As it can be clearly seen, the model captures the exponential decay of the afferent signal reasonably good. The time crossing zero values for both cases are approximately 16.5 seconds and the peak values of the sensor response are approximately equal to 0.235 rad/s for the same stimulus. For this verification step, the SCC transfer function is converted to its state-space representation using the Matlab built-in functions.
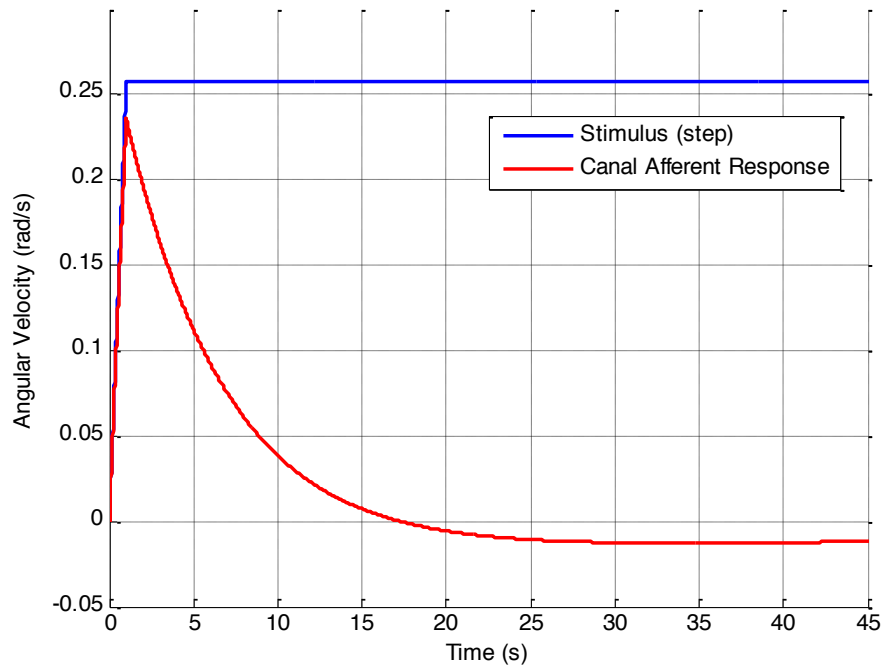
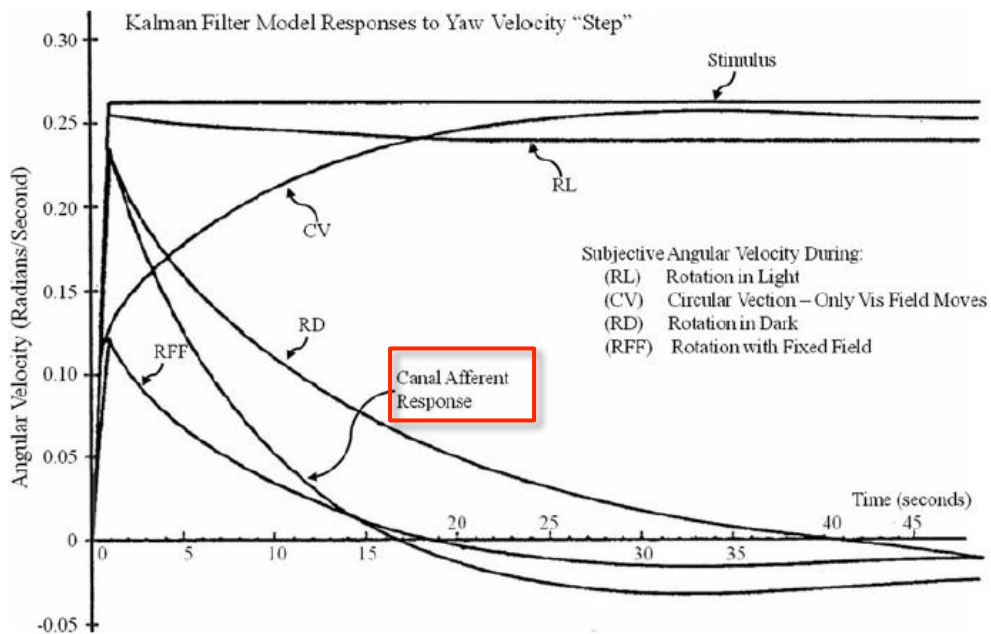***Figure 16:*** *Implemented SCC model's response to a step stimulus*

Figure 17: *Borah et al.'s orientation model responses to a step angular velocity stimulus.*
The SCC model output is highlighted [18].

In the Figure 18, on the other hand, a similar scenario is produced in the aircraft simulation that is linked to the MBO. In this verification step, implementation of the sensor dynamics and its coherence with the linked aircraft model is being verified. Again, the afferent signal of the implemented model decays towards zero.
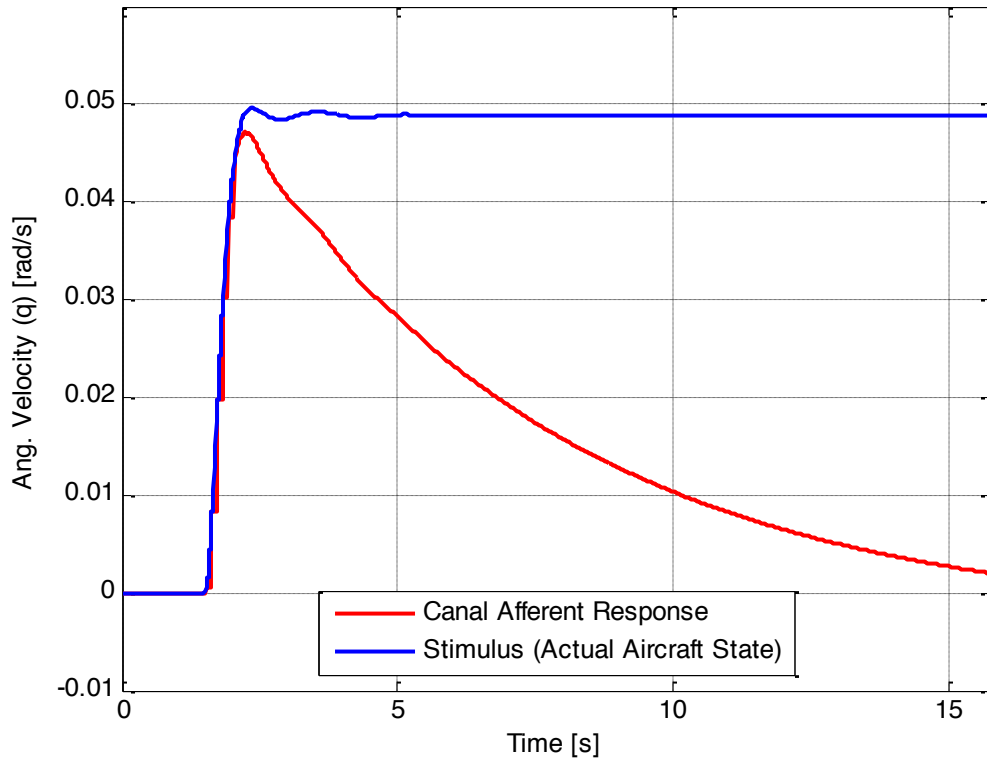

Figure 18: Implemented SCC model's response to a banking maneuver (from aircraft model that is linked to the MBO)

The SCC outputs are ambiguous in the cases of sub-threshold maneuvers. The SCC models, therefore, are known to provide no information when the maneuvers are performed below the threshold. However, it is not clear whether the SCC becomes inactive (e.g., there is no continuous measurement (**y**) provided) or simply provides zero measurements to the MBO (e.g., **y** = 0) during sub-threshold motions. To investigate this issue, experimental studies were conducted using the MBO. For this purpose, sub and above-threshold bank and pitch maneuvers were simulated with two different

configurations: (1) the SCC providing zero measurement, and (2) the SCC becoming inactive in the sub-threshold motions. The maneuver starts at 5 seconds into the run. The top graph in Figure 19 (1) shows the 2-sigma bounds for the zero measurement case and the lower graph (2) shows the 2-sigma bounds when the SCC becomes inactive and does not provide any measurements to the MBO. As it can be seen from (2), the inactive SCC reflects on the 2-sigma bounds. The 2-sigma bounds, in the inactive SCC case (2), grow as if there is no sensor before the above-threshold maneuver kicks in. On the other hand, the zero measurement case (1) still takes into account the presence of a sensory system, and thus, does not grow as much as the case (1).

Although the SCC provides inaccurate information during the sub-threshold motions, its presence cannot be ignored. Therefore, the MBO applies the case (1), and implements an SCC model that feeds zero measurement when the motion is below the threshold.

(1) The SCC provides zero measurement
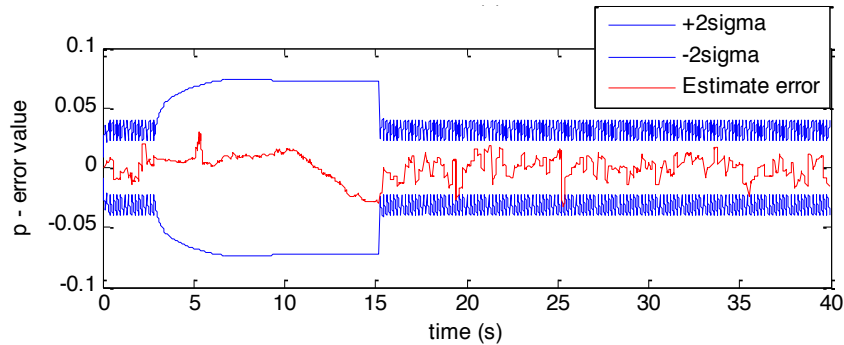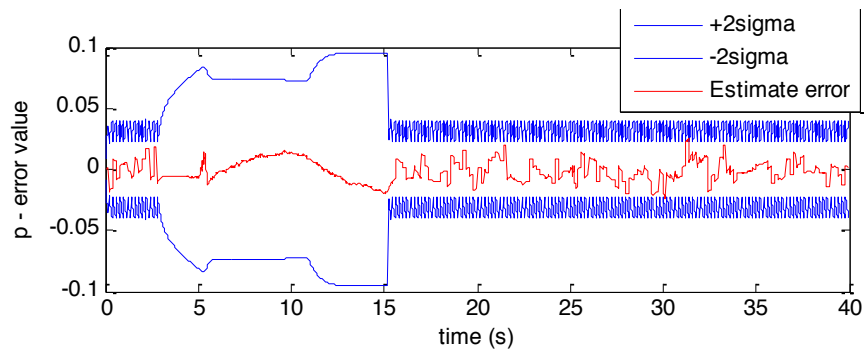

(2) The SCC becomes inactive

Figure 19: *Experimental studies on the SCC measurements for sub-threshold cases. In this case an above-threshold bank maneuver is initiaed at 5th second. Two different configurations for the SCC measurements are illustrated.*

The Figure 20 shows the model outputs in case of a sub and above threshold angular maneuver. Since the SCC doesn't provide any information sub-threshold, afferences (or canal firing rates) do not respond to the maneuver. This verifies that the SCC provides correct sensory outputs (canal firing rates) both for sub-threshold and for above-threshold cases.
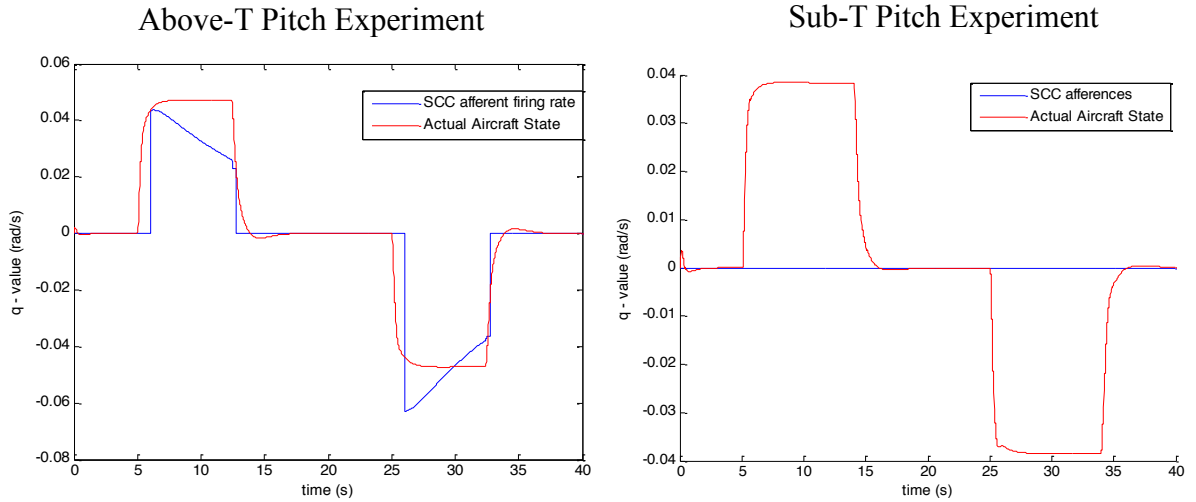
Figure 20: The SCC model outputs (afferences) during sub-threshold and above-threshold pitch maneuvers

4.2.3 The Otolith Model

Similar to the SCC model, the otolith model implemented to the MBO is also based on a previously developed model, built by Grant and Best [13]. The existing otolith models' fidelity are not as high as the SCC models. There is no robust information on otolith afferences in the literature that can be compared with the implemented model responses. Thus, this verification examined whether the otolith model, by first principles, measures the specific force correctly.

The specific force in x-axis: $-\theta.g - \dot{u}$

Figure 21 illustrates the otolith model response during a *no-pitch forward acceleration* experiment. The otolith model response does make sense due to the contrary behavior between the x-component of the acceleration ($\dot{u}$) and the corresponding component of the otolith response (specific force in x-component). The pitch angle (θ) does not change and equal to zero degree and, thus, does not contribute to the otolith measurement.
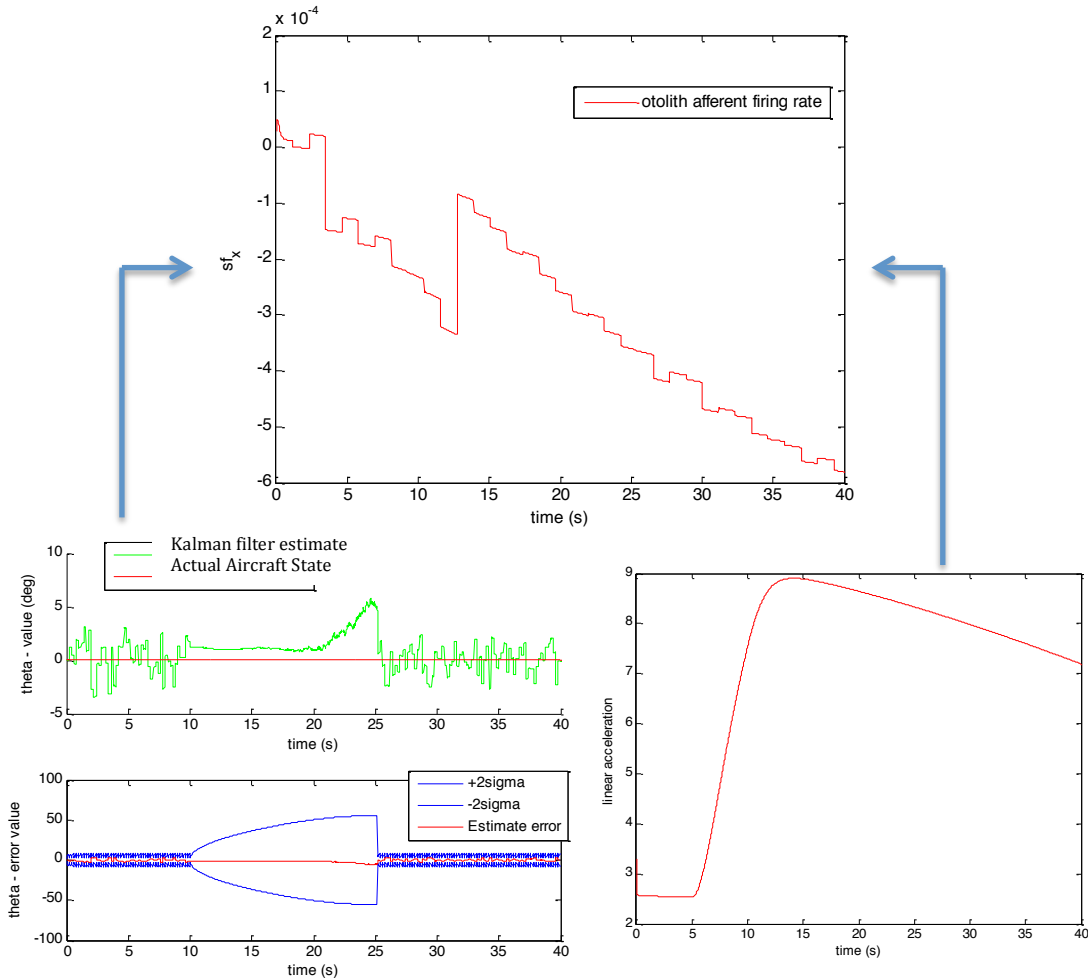
51

Figure 21: *The implemented otolith model response (afferent firing rate) in case of a no-pitch forward acceleration maneuver.*

Figure 22 illustrates the otolith model response during an above-threshold *pitch-up* experiment. As it can be seen from the bottom right graph, a deceleration is observed due to the nature of aircraft dynamics. The otolith model response in this pitch-up case also makes sense as the afferent firing rate complies with the specific force relationship stated above. These figures verify the otolith responses, in various maneuvers, provide the accurate measurements to the MBO defined by the specific force relationship.
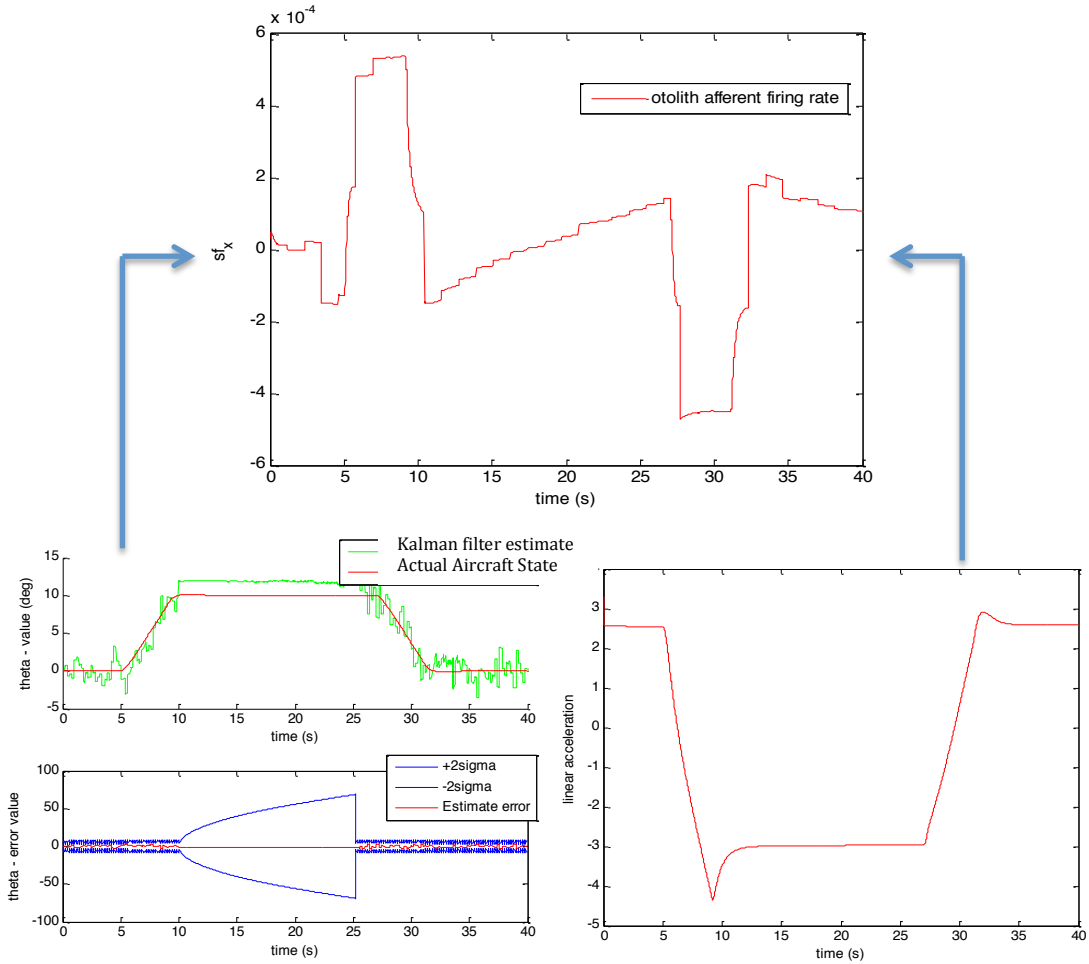
Figure 22: *The implemented otolith model response (afferent firing rate) in case of an above-threshold pitch-up maneuver.*

In addition to the preliminary verification of the otolith, an experimental study examined the otolith model to justify the otolith measurement matrix ($\mathbf{C_{OTO}}$) that should be used in the MBO. Three different flight conditions are examined using two different variation of otolith measurement matrix (C_{REAL} & $C_{LEARNED}$).

Two different otolith measurement matrix configurations were generated using these two variations of otolith measurement matrices. The first configuration uses the same measurement matrix (C_{REAL}), generated through linearization of the internal sensor dynamics, for both aircraft side and pilot side of the MBO. The second configuration applies the same measurement matrix (C_{REAL}) generated through linearization for the

aircraft side, and a modified matrix (C_{LEARNED}) for the pilot side of the MBO. The (C_{LEARNED}) case may represent an otolith measurement matrix of a subject that has learned the otolith sensory dynamics through experiencing certain motions. The C_{LEARNED} matrix for can be generated based on the actual measurement matrix C_{REAL}, and can be modified for the experimentation purposes. In this experimentation study, it is assumed that the C_{LEARNED} only contains the angel relationships of the otolith dynamics. In other word, this particular experiment simulates an otolith measurement matrix that has been learned primarily by experiencing angular motions. To generate this particular C_{LEARNED}, all off the elements of C_{REAL} is set to zero except for the quaternion relationships.

In this study, (f1) no acceleration 20 degrees pitch-up, (f2) forward acceleration with no pitch, and (f3) forward acceleration with 20 degrees pitch-up were the three flight conditions.

As it can be seen from Figure 23, the pitch rates, pitch angles, and forward component of the airspeed is compared using two measurement matrix configurations (C_{REAL}) & (C_{LEARNED}). Although results look similar, (C_{REAL}) configuration exhibits much smooth pilot expectation for all the shown states. The (C_{LEARNED}) configurations rapid changes in some cases even caused the estimation error to exceed the 2-sigma bounds, since the residuals are calculated by comparing real and estimated measures created in two different ways.
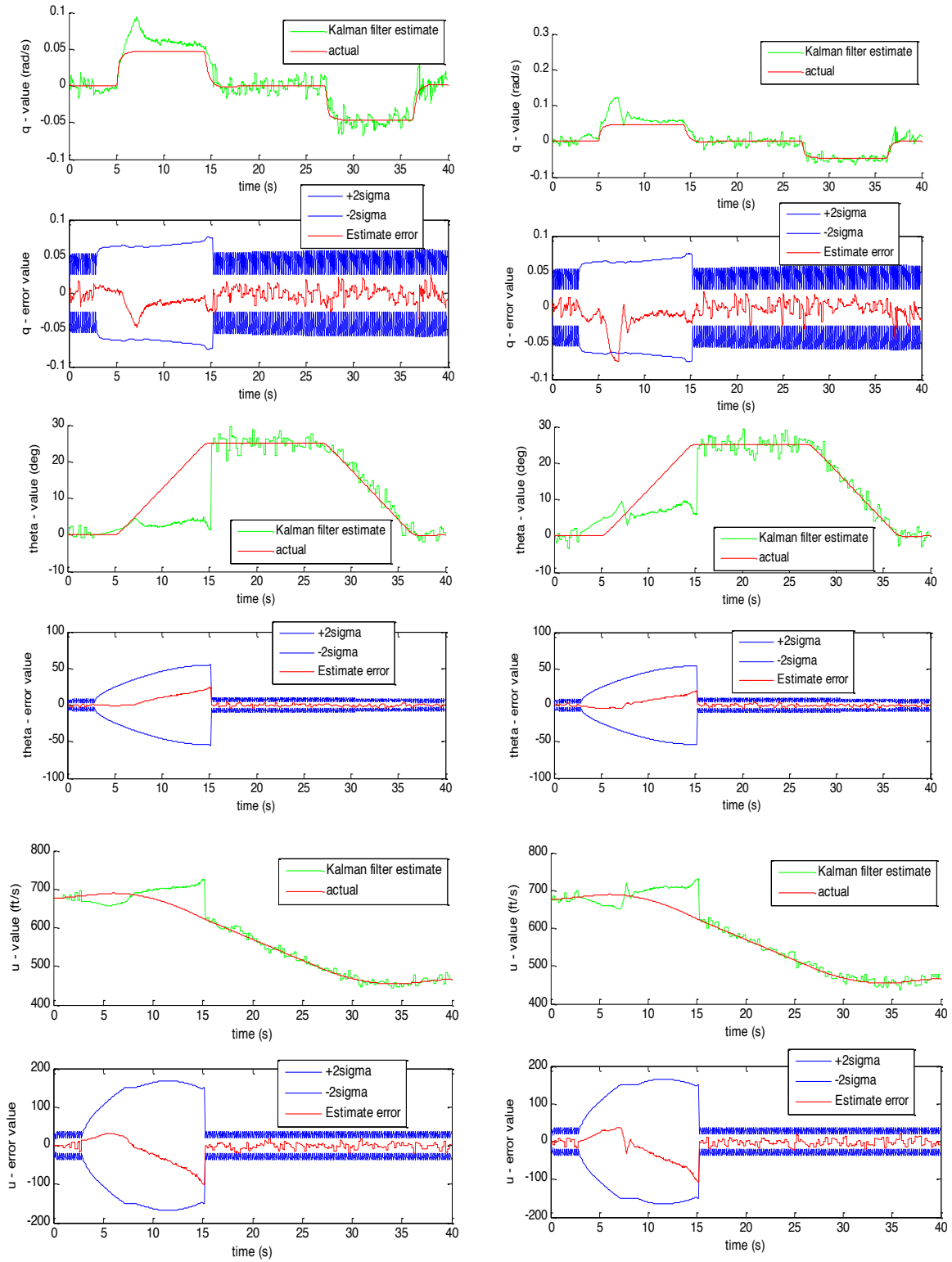
Figure 23: *Otolith experimental study - No acceleration, pitch-up (f1) flight condition with (C_{REAL}) on the left & ($C_{LEARNED}$) on the right*

In Figure 24, the pitch angle values of both configurations are compared. The second configuration ($C_{LEARNED}$) was aiming to capture a better angle expectation and more explicit vestibular illusions. Although they both reproduce the somatogravic illusion to some degree, the first configuration (C_{REAL}) seems to be exhibiting more consistent behavior if the expectation, and thus, reproduce the somatogravic illusion more clearly.
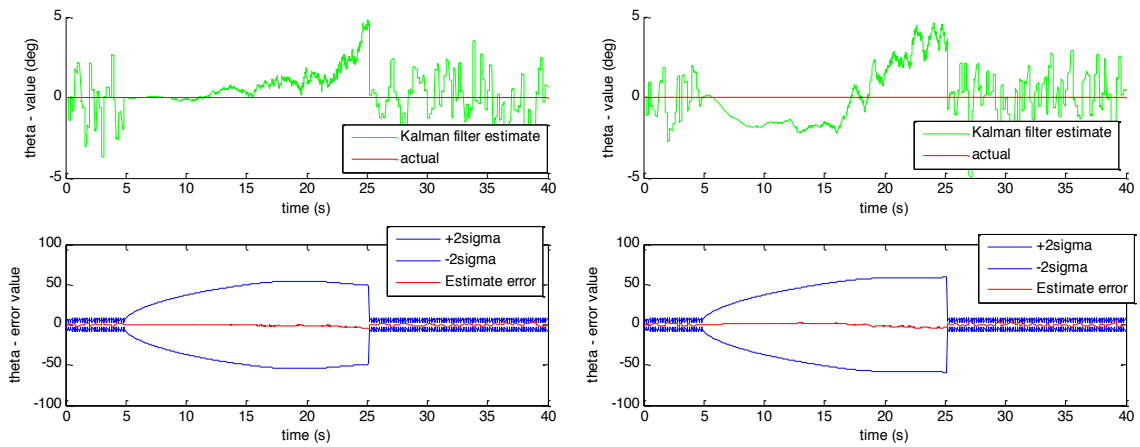

Figure 24: *Otolith experimental study - Forward acceleration, no pitch-up (f2) flight condition with (c1) on the left & ($C_{LEARNED}$) on the right*

The third flight condition (f3) combines the first two flight conditions (f1) & (f2). Again, the pitch rates, pitch angles, and forward component of the airspeed can be seen for both configurations (C_{REAL}) & ($C_{LEARNED}$) in Figure 25. The 2-sigma bounds do not exhibit any differences for both configurations. The best possible pilot expectations, on the other hand, show the similar smooth behavior in the (f3), and thus, keep the estimation errors within the 2-bounds for the first configuration (C_{REAL}).
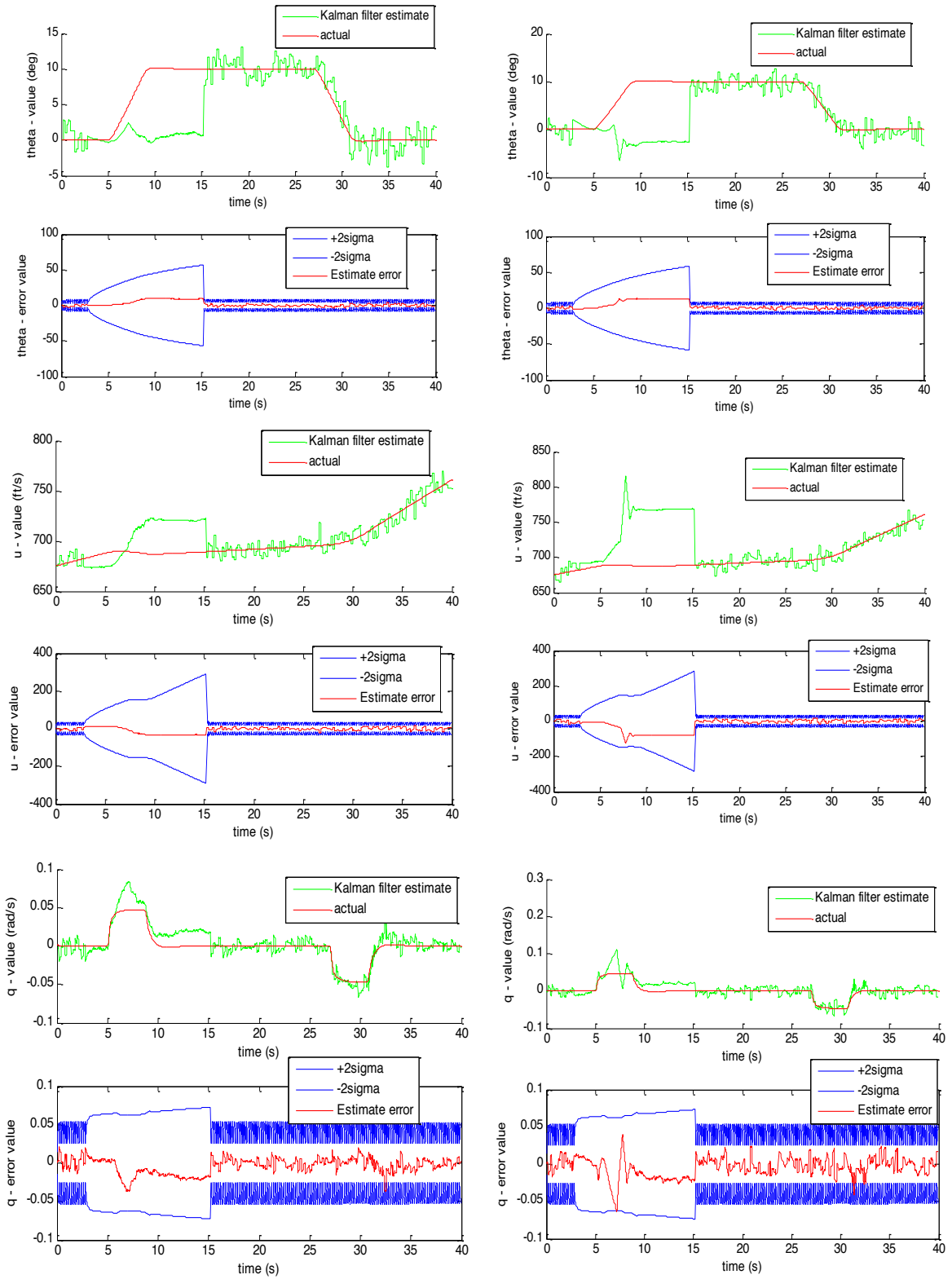
Figure 25: *Otolith experimental study - Forward acceleration, pitch-up (f3) flight condition with (C$_{REAL}$) on the left & (C$_{LEARNED}$) on the right*

57

This experimental study was aiming to investigate the effects of different measurement matrices on the best possible pilot expectation. The modified C_{LEARNED} matrices generate different measurement estimates than the actual measurements defined by the sensor dynamics, which might cause substantially different expectations of the states. Conceptually, using the C_{REAL} configuration represents a pilot that learned the otolith sensory dynamics fully through experiencing all types of forces and rotations experienced during natural 1-g motions (e.g., walking, sitting, running, etc.). Since the C_{REAL} is generated through the validated otolith models, it is known to some degree. Therefore, the MBO applies the C_{REAL} configuration, which implements the same measurement matrix for both the aircraft and for the pilot aspect of the MBO. However, this experimentation opens up new research questions on types of C_{LEARNED} matrices that best capture the illusions.

4.2.4 The Dryden Model

The Dryden Model has been implemented to simulate gusts acting on the simulated aircraft linked to the MBO. To verify the implementation, the model responses were compared to the results of the built-in Matlab Dryden Model. The time history graphs of the all three components of the linear (v_x, v_y, v_z) and angular (w_x, w_y, w_z) gusts for various turbulence intensities (light, moderate, severe) are plotted. Using these gust vales, an Fast Fourier Transform (FFT) analysis verified that Matlab built-in function results match with the implemented Dryden Model results in the frequency domain.

As an example, the comparison graphs only for the linear velocity gusts and angular velocity gusts produced by in severe turbulence level are presented in Figure 26 and in Figure 26, respectively. To verify the Dryden Model, the same analyses are conducted for all the turbulence intensities.
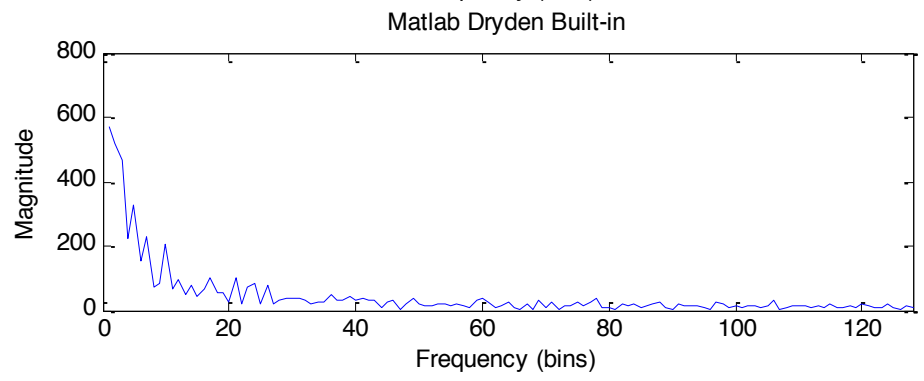
Figure 26: *Linear gust values in severe turbulence. Comparison between the Matlab built-in function and WMC implementations (Time-history and Frequency Spectrum Distribution)*

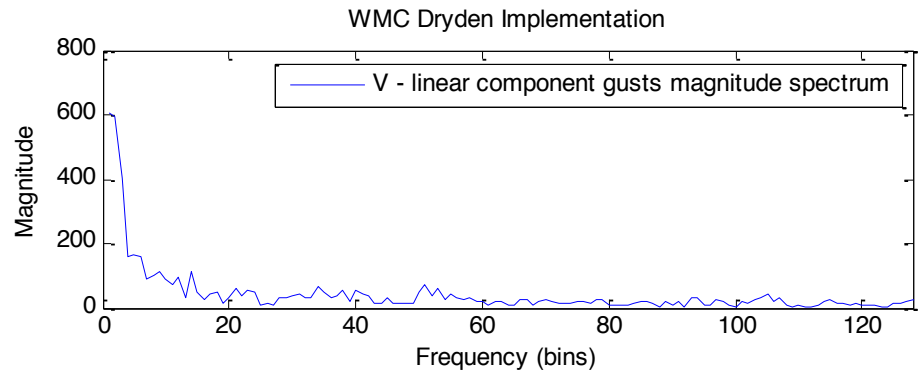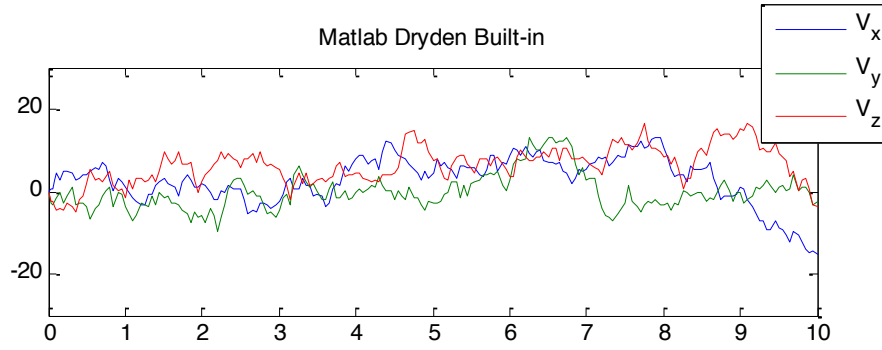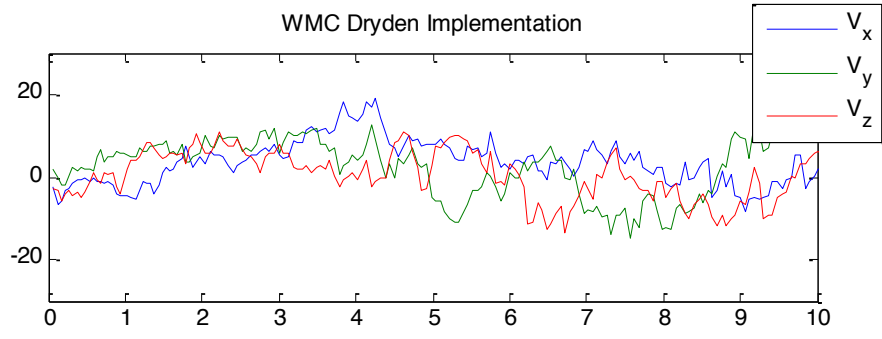***Figure 27:*** *Angular gust values in severe turbulence. Comparison between the Matlab built-in function and WMC implementations (Time-history and Frequency Spectrum Distribution)*
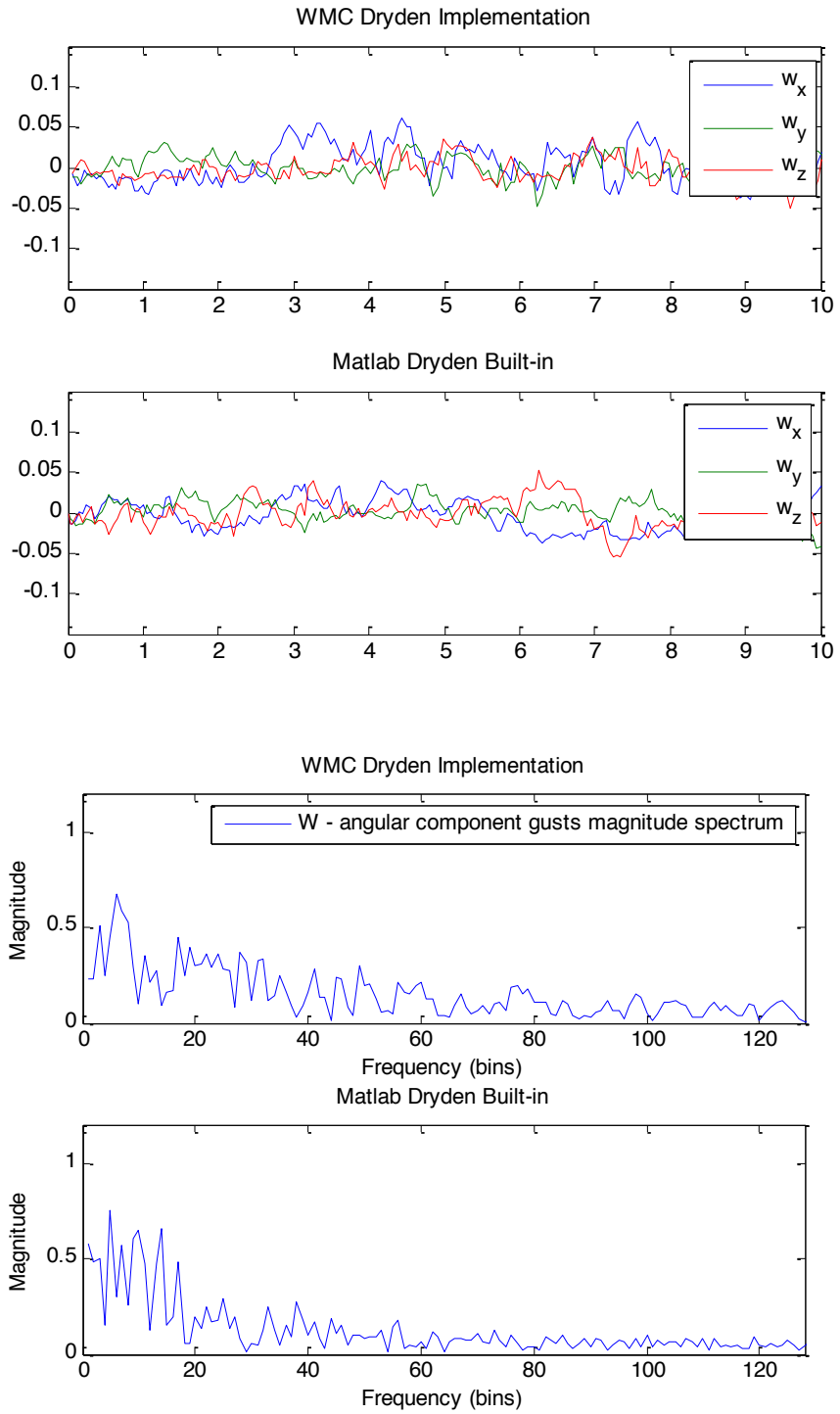
60

4.3 Validation of the Integrated MBO

The validation process deals with the ability of the model to predict known problems with pilot SD. Specifically, the MBO is expected to reproduce the illusions that occur due to vestibular limitations. Certain maneuvers without visual correction of the MBO's estimate are associated with some of the vestibular illusions. For instance, a maneuver below the SCC threshold does not sense angular velocity and thus, cause a *somatogyral illusion*. Likewise, in the case of a linear forward acceleration maneuver, the pilot's best possible expectation is expected to show a pitch-up sensation due to *somatogravic illusion*. These vestibular illusions are reproduced by the MBO and are illustrated in the next sub-sections. These sub-sections then confirm that the MBO correctly integrates all measurements to also reproduce visual correction of illusions.

4.3.1 Somatogyral Illusions and Impact of Visual Correction

Figure 28 and 29 is show a same banking maneuver except that the maneuver is sub-threshold in Figure 28 and above-threshold in Figure 29. In both cases, pilot is distracted onset of the maneuver such that there is no visual information from 3rd to 15th seconds. In Figure 28, the MBO's estimation reflects the sub-threshold maneuver causing *somatogyral illusion.* The SCC's contribution to the angular motion sensation can be clearly seen in Figure 29: Even though there is no visual correction present at the beginning of the maneuver, the MBO's estimate is able to capture the roll rate to some degree.
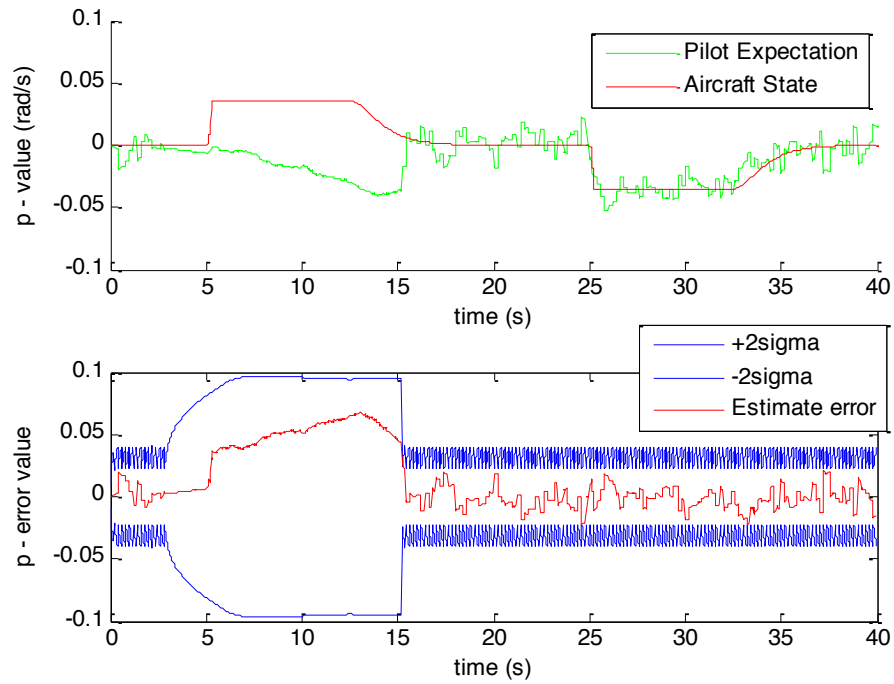
Figure 28: *Roll rate state and its expectation during a sub-threshold bank maneuver (Distraction from 3rd to 15th sec - No visual scanning at the beginning of the maneuver).*
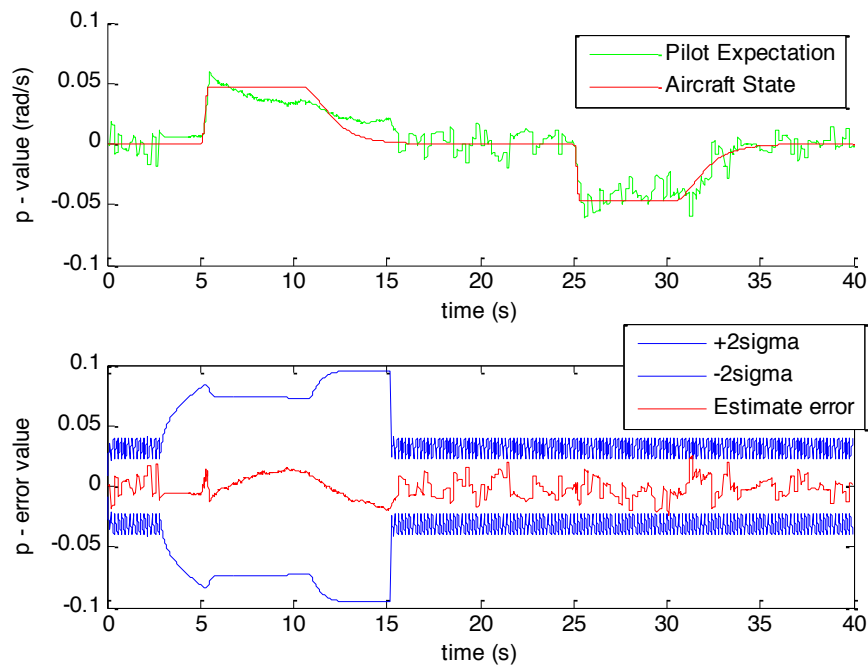

Figure 29: *Roll rate state and its expectation during an above-threshold bank maneuver (Distraction from 3rd to 15th sec - No visual scanning at the beginning of the maneuver).*

As discussed earlier in *Chapter 2: Background,* the vestibular illusions occur when the visual cues are lacking. This indicates the power of proper visual scanning of instruments when the outside visual field is not available to the pilot. Since spatial disorientation is not likely to occur with a proper scan pattern, the model estimates of the aircraft state responses are expected to show no significant divergence from the actual aircraft state in case of a proper scanning pattern.

The following illustrates the same scenarios shown in Figures 28 and 29, which are known to be prone to SD, with a recursive T-Scan scan-pattern. Its recursion can be varied but for simplicity it is assumed that the instruments are scanned every second. In Figures 30 and 31, the roll experiment shown in Figure 28 and 29 is run once more with a proper T-Scan. Having the visual cues help pilot expectation to capture the actual aircraft states relatively better and thus, helps avoid the illusions that might end up causing SD. As it can be seen from both figures, there is not much of a difference the way the pilot's best possible expectation behaves. Figure 31 expectation shows a slight decay around 5th to 10th seconds, which might be due to the decaying behavior of the SCC afferences activated due to an above-threshold roll maneuver.
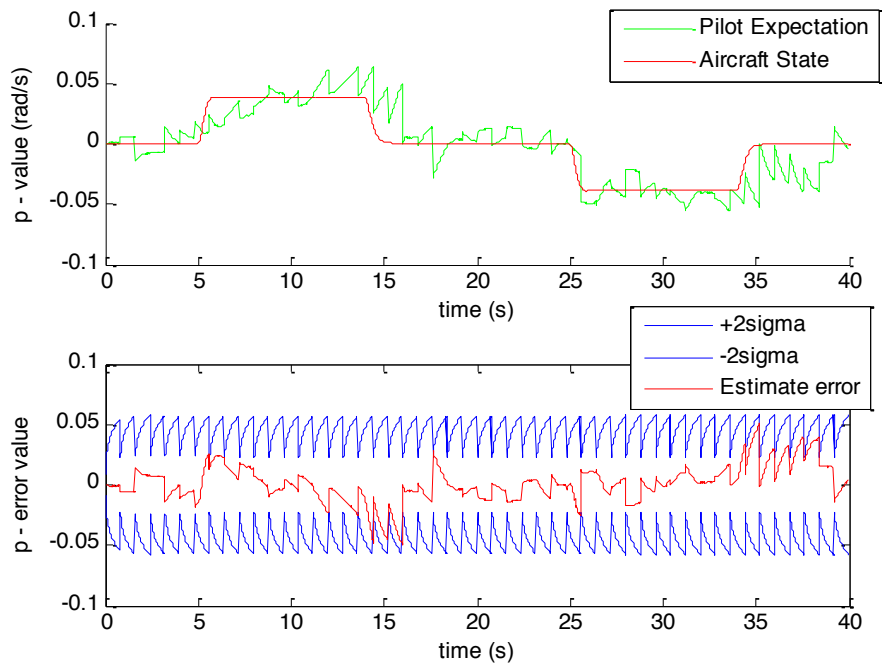
Figure 30: *Roll rate state and its expectation during a sub-threshold bank maneuver with a proper T-Scan scanning pattern.*
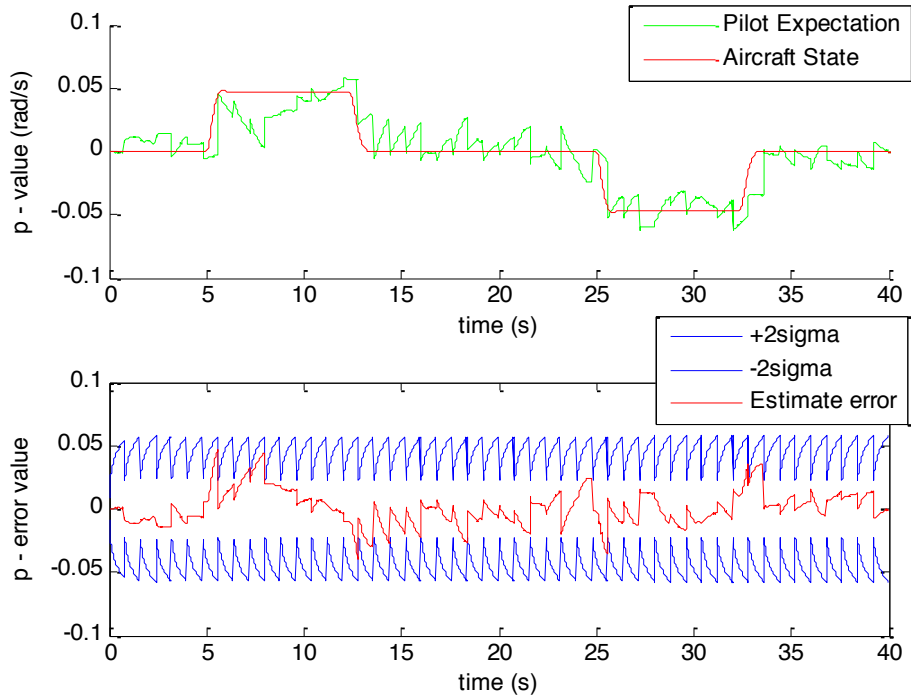

Figure 31: *Roll rate state and its expectation during an above-threshold bank maneuver with a proper T-Scan scanning pattern.*

4.3.2 Somatogravic Illusions and Impact of Visual Correction

Considered to be one of the most common and dangerous illusions in context of spatial disorientation, the *somatogravic illusion* is a crucial element of orientation models: Linear accelerations and decelerations, without visual correction, lead to pitch-up and pitch-down sensations, respectively. So, a useful model needs to be capable of reproducing this illusion.

The somatogravic illusion captured from the proposed model is represented in Figures 32 and 33. Figure 32 shows a *no-pitch linear acceleration* case. The linear acceleration, here, is in the x-axis of the aircraft. There is a 15 second distraction starting at the 15th second into the simulation, which causes a slight pitch-up sensation, building up as distraction time goes by, due to the otolith sensor's coupled specific force measurements. The time-history plot of the acceleration can be seen on the right-hand side of the same figure.

Conversely, Figure 33 shows a *no-pitch linear deceleration* maneuver with 15 seconds of distraction starting from the 15th second. As it can be seen from the graph, the pilot starts sensing a pitch-down a few seconds into the distraction. Lack of visual cues leads pilot to sense the aircraft state solely based on his/her vestibular sensor and thus, to experience the somatogravic illusion. Again, the time-history of the deceleration is located on the right-hand side of the figure.
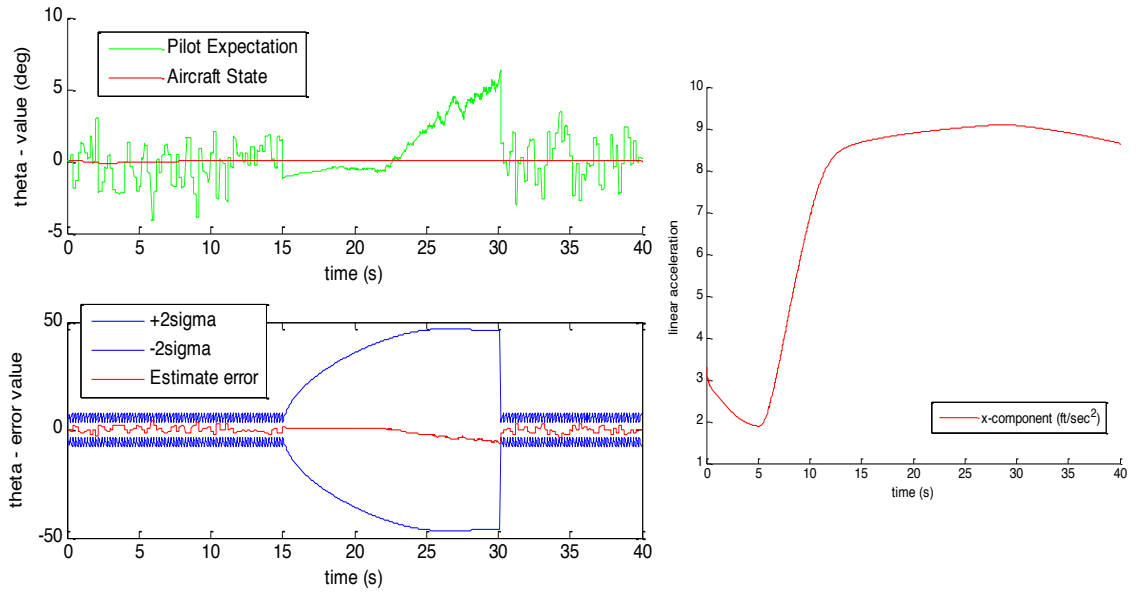
Figure 32: *Somatogravic illusion: pitch-up sensation - Pitch angle and its expectation during an acceleration (no-pitch) maneuver (Distraction from 15th to 30th sec).*
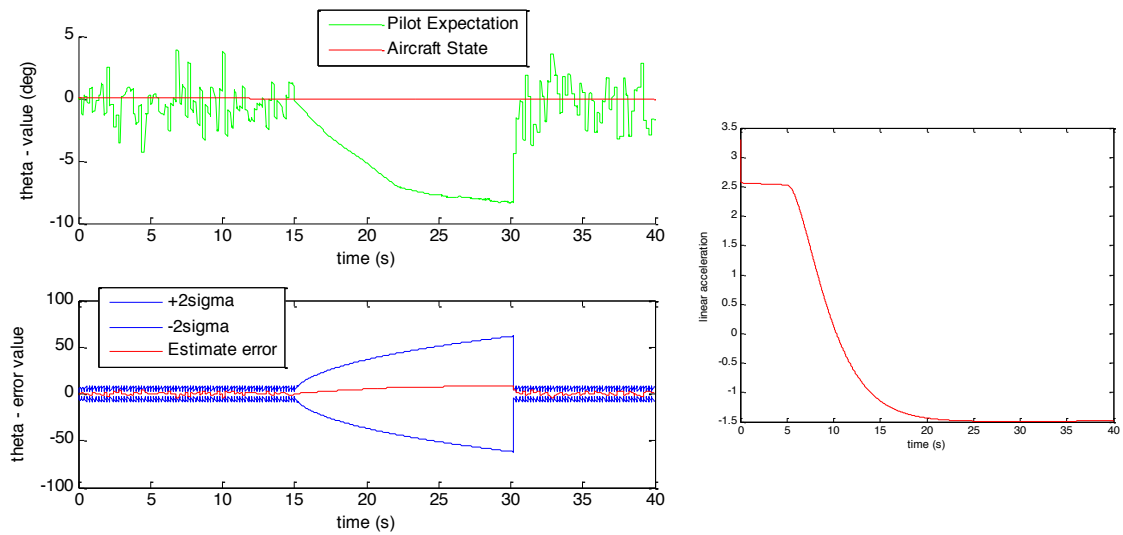

Figure 33: *Somatogravic illusion: pitch-down sensation - Pitch angle and its expectation during a deceleration (no-pitch) maneuver (Distraction from 3rd to 15th sec).*

There are coupling for some of the aircraft states. Therefore, when the MBO has the correct model of the aircraft system dynamics in its internal simulation, coupling should between the expected states. For instance, when the expectation of the vertical speed indicating a positive value (downward direction), the MBO's estimates of the altitude state should be going down (losing altitude sensation). According to this, if the forward component of the airspeed is examined in the case of an acceleration maneuver, seen in Figure 32, pitching-up sensation is causing it to diverge from the actual aircraft airspeed state (Figure 34).
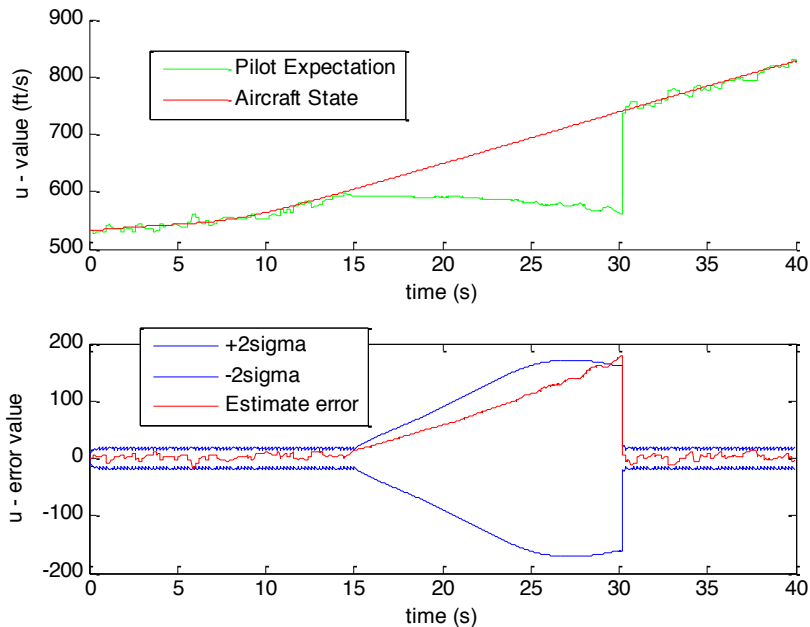
Figure 34: *Somatogravic illusions effect on the other states - Airspeed and its expectation during an acceleration (no-pitch) maneuver (Distraction from 15th to 30th sec).*

Figures 35 and 36 are the same maneuvers executed in Figures 32 and 34, except with a proper T-Scan. The significance of the visual cues is apparent in the sense that there is no somatogravic illusion with the proper instrument scanning.

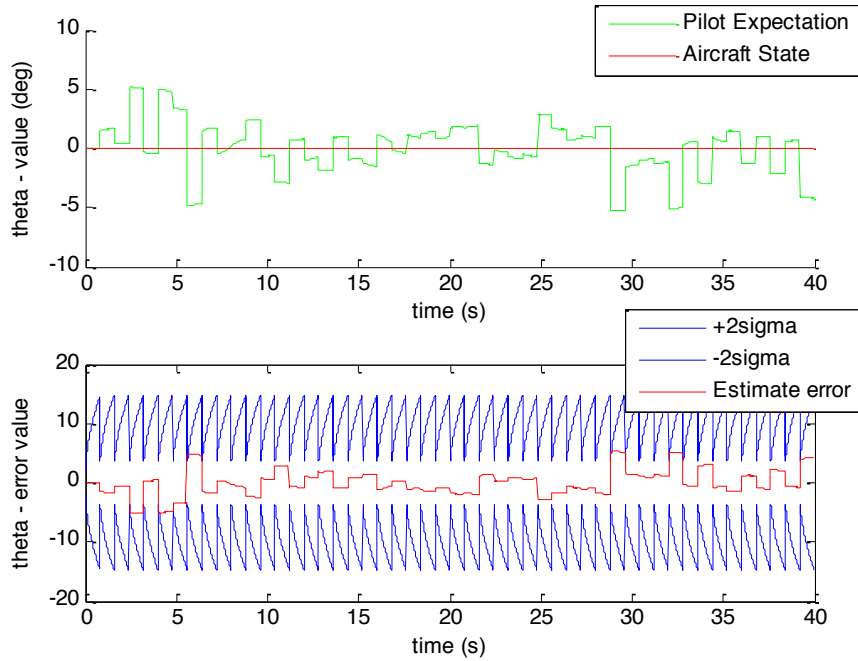***Figure 35:*** *Somatogravic Illusion Correction with a T-Scan - Pitch angle and its expectation during an acceleration (no-pitch) maneuver.*
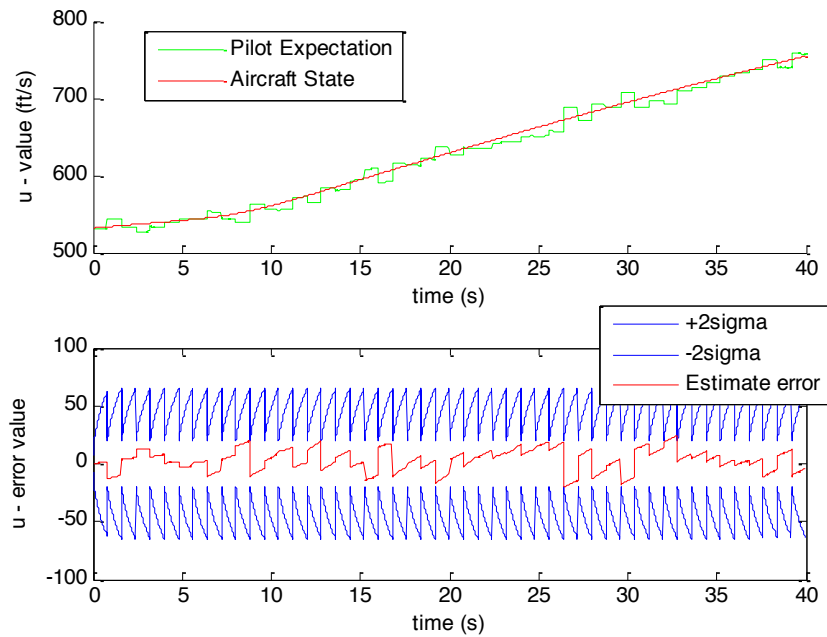

Figure 36: *Somatogravic illusion Correction with a T-Scan – Forward component of the airspeed and its expectation during an acceleration (no-pitch) maneuver.*

CHAPTER 5

CONCLUSION

5.1 Summary

This thesis demonstrates the structure and development of a model-based observer (MBO) that can predict the best-possible pilot expectation of aircraft state given accurate knowledge of the aircraft dynamics, vestibular sensing, and a given visual scan. The MBO is applicable to a wide range of potential conditions and variations in pilot instrument scanning behavior, which makes it possible to investigate the underlying mechanisms of spatial disorientation (SD). Additionally, the model accounts for the expert pilot's knowledge of the aircraft's dynamics. While this thesis demonstrated only the effects of visual scanning and vestibular system on the pilot's best possible expectation, the model can be extended to examine the a large space of potential contributions to the best possible pilot expectation.

One engineering utility of this model is to identify the visual scanning behavior required of the pilot with any SD countermeasure. Thus, it can be used by designers to gain design insights for the development of novel flight deck display design(s) by providing them a structured method for predicting the best possible pilot expectation given some estimated uncertainty due to the combined effects of aircraft sensor error, uncertainty or noise added by the display (e.g., the precision with which it may be interpreted), and any perceptual error inherent to the pilot. Thus, display improvements in terms of reduced uncertainty, and other designs such as alerting the pilot's attention, can be analyzed rigorously and quantitatively. These computational simulations, by running faster than real-time, can assess a large space of combinations of flight maneuvers, disturbance levels (wind gusts) and visual scans. Similarly, engineering design may use

69

such simulations to identify problematic flight conditions particularly susceptible to poor pilot expectation of aircraft state.

Additionally, eye-tracking measures from human-in-the-loop (HITL) simulations can be used to estimate the best possible estimates that the pilots could have during a particular maneuver. In the future, the potential further exists to use the MBO in real-time, with knowledge of actual pilot scan provided by eye-tracking, to assess the best possible pilot expectation of aircraft state resulting from their actual recent visual scan, again to alert the pilot or actively control the salience of important information.

5.2 Contributions

The contribution of this thesis is to establish a computational model that can predict the best possible pilot expectation of aircraft state based on vestibular cues and a given visual scan. Uniquely, the MBO also accounts for pilot expertise, and thus, can predict the best possible pilot expectation of the aircraft states.

The visual and vestibular models implemented in the MBO have generic structures, which can be modified. Thus, if a new and more applicable vestibular model is developed, the new vestibular dynamics can easily be redefined in the implemented model structure. Having the generic structure also helps the eye-tracking data to be swapped in to the visual scanning model, and thus, allows the model to be used real-time based on actual pilot scan pattern of the flight instruments.

By applying the model to a wide range of potential conditions and variations in the pilot's visual scan-behavior, it is possible to investigate the information requirements of the pilot and underlying mechanisms of SD. This computational model makes it possible to examine the full space of variations in these mechanisms through 'what-if' experiments that identify those mechanisms with the greatest potential for triggering SD.

The model can, thus, be used to provide a structured, predictive basis for development of novel flight deck display design(s) and/or other flight deck technology

intervention(s). The model can help identify the critical SD mechanisms, and thus, help identify which countermeasures may best help prevent SD. For instance, one of the known mechanisms of SD is distraction. The model predicts the impact on best possible pilot expectation of a visual scan that stops visual sampling at some key point in the flight. Key points of distraction during maneuvers and problematic durations of distraction can, thus, be identified. Likewise, the impact of the accuracy with which a pilot can perceive information from a flight instrument can also be characterized.

Another design intervention that the MBO can help evaluate is the positioning and design of the displays to mitigate the time required to observe and to interpret the displayed information. In subsequent flight simulator and/or flight test evaluations, these design interventions can then also be measured in terms of whether pilots actually demonstrate these expected visual sampling behaviors.

5.3 Future Work

Some of the aspects of the developed model can still be enhanced and/or improved to make it more computationally efficient. Built in a simulation framework (WMC) in C++, improving the computational efficiency will foster current efforts to run the model on-line. For on-line prediction of the best-possible pilot expectation, the model can be coupled with an HITL aircraft simulator. The subject's gaze, in the HITL simulator, can be traced with the help of an eye-tracker. This would allow the model to get the sampling information from the eye-tracker and trigger the corresponding visual sampling scan-actions. Eventually, such a capability may also be used on board aircraft.

Additionally, new sensory systems can be incorporated to increase the accuracy of the pilot expectation prediction. For instance, a model of the proprioceptive system, and more elaborate vestibular models, could be implemented. Although both the proprioceptive system and the otolith measure inertial forces, this redundancy might help reduce the variance of the estimation error for some cases. In addition to proprioceptive

sensors, a continuous visual measurement model can also be implemented to take into account the out-of-the-window visual cues for clear sky, daytime flight scenarios.

REFERENCES

[1]   Bateman, Don. "Some Thoughts on Reducing the Risk of Aircraft Loss of Control." *AIAA Aircraft Loss of Control. Session III: Potential System Solutions. Toronto, Canada* (2010).

[2]   Airplanes, Boeing Commercial. "Statistical Summary of Commercial Jet Airplane Accidents: Worldwide Operations 1959-2011." *Aviation Safety, Boeing Commercial Airlines, Seattle, Washington* (2013).

[3]   Previc, Fred H., and William R. Ercoline, eds. *Spatial disorientation in aviation – Chapter 5*. Vol. 203. Aiaa, 2004.

[4]   Gibb, Randy, Bill Ercoline, and Lauren Scharff. "Spatial disorientation: decades of pilot fatalities." *Aviation, space, and environmental medicine* 82.7 (2011): 717-724.

[5]   "Situational Awareness." *SKYbrary*. N.p., n.d. Web. 12 July 2013. <http://www.skybrary.aero/index.php/Situational_Awareness_(OGHFA_BN)>.

[6]   Endsley, Mica R. "Design and evaluation for situation awareness enhancement." *Proceedings of the Human Factors and Ergonomics Society Annual Meeting*. Vol. 32. No. 2. SAGE Publications, 1988.

[7]   Newman, David G. *An overview of spatial disorientation as a factor in aviation accidents and incidents*. No. B2007/0063. Australian Transport Safety Bureau, 2007.

[8]   Bryan, Leslie Aulls. "180-degree turn experiment." No. 11. Aviation Ground School. Urbana, Ill.: Institute of Aviation. University of Illinois at Urbana-Champaign, 1954

[9]   Bürki-Cohen, J. and Sparko, A.L. Airplane Upset Prevention Research Needs, *AIAA Modeling and Simulation Technologies Conference and Exhibit*, 2008.

[10]   Newman M. C, Newman, Michael C., et al. "The Role of Perceptual Modeling in the Understanding of Spatial Disorientation During Flight and Ground-based Simulator Training." *AIAA Modeling and Simulation Technologies Conference, 2012*

[11]   Dahleh, Munther. "6.241 Dynamic Systems & Control, Fall 2003." (2003).

[12]   Previc, Fred H., and William R. Ercoline, eds. *Spatial disorientation in aviation – Chapter 2*. Vol. 203. AIAA, 2004.

[13]   Pommellet, Pierre Eric. *Suboptimal estimator for the spatial orientation of a pilot*. Diss. Massachusetts Institute of Technology, 1990.

[14]   Kleinman, D.L., Baron, S. and Levison, W.H. An Optimal Control Model of Human Response Part I: Theory and Validation. *Automatica, 6*, 357-369. 1970.

[15]   Baron, Sheldon, D. L. Kleinman, and W. H. Levison. "An optimal control model of human response part II: prediction of human performance in a complex task." *Automatica* 6.3 (1970): 371-383.

[16]   Baloh, Robert W., and Kevin Kerber. *Baloh and Honrubia's Clinical Neurophysiology of the Vestibular System*. Vol. 77. Oxford university press, 2010.

[17]   Grant, J. Wallace, and William A. Best. "Mechanics of the otolith organ-dynamic response." *Annals of biomedical engineering* 14.3 (1986): 241-256.

[18]   Borah, Joshua, Laurence R. Young, and Renwick E. Curry. "Optimal estimator model for human spatial orientation." *Annals of the New York Academy of Sciences* 545.1 (1988): 51-73.

[19]   Young, Laurence R. "Optimal estimator models for spatial orientation and vestibular nystagmus." *Experimental brain research* 210.3-4 (2011): 465-476.

[20]   Merfeld, Daniel M., et al. "A multidimensional model of the effect of gravity on the spatial orientation of the monkey." *Journal of vestibular research: equilibrium & orientation* (1993).

[21]   Newman, Michael Charles. *A multisensory observer model for human spatial orientation perception*. Diss. Massachusetts Institute of Technology, 2009.

[22]   Kleinman, D.L. and Curry, R.E. Some New Control Theoretic Models for Human Operator Display Monitoring. *IEEE Transactions on Systems, Man and Cybernetics*, *SMC-7*(11), 778-784, 1977.

[23]   Pritchett, Amy R., and Karen M. Feigh. "Simulating first-principles models of situated human performance." *Cognitive Methods in Situation Awareness and Decision Support (CogSIMA), 2011 IEEE First International Multi-Disciplinary Conference on*. IEEE, 2011.

[24]   Jessie, C. "Implementation and Testing of Turbulence Models for the F18-HARV Simulation." (1998).

[25]   Hoffman, William C. "A Pilot Model with Visual and Motion." (1976).

[26]   Simon, Dan. *Optimal state estimation: Kalman, H infinity, and nonlinear approaches*. Wiley.com, 2006.

[27]   MacNeilage, Paul R., Narayan Ganesan, and Dora E. Angelaki. "Computational approaches to spatial orientation: from transfer functions to dynamic Bayesian inference." J *Neurophysiol* 100 (2008): 2981-2996.

[28]   Mosby, E. "Mosby's medical dictionary." 8th edition, (2009), Elsevier.

[29]   Angelaki, Dora E., and Kathleen E. Cullen. "Vestibular system: the many facets of a multimodal sense." *Annu. Rev. Neurosci.* 31 (2008): 125-150.

[30]   Fernandez, Cesar, and Jay M. Goldberg. "Physiology of peripheral neurons innervating otolith organs of the squirrel monkey. II. Directional selectivity and force-response relations." *J Neurophysiol* 39.5 (1976): 985-995.

[31]   Small, Ronald L., et al. *Multisensory integration for pilot spatial orientation*. MICRO ANALYSIS AND DESIGN BOULDER CO, 2006.

[32]   "Vestibular System and Illusions." *SKYbrary*. N.p., n.d. Web. <http://www.skybrary.aero/index.php/Vestibular_System_and_Illusions_(OGHF A_BN)>

[33]   Karwowski, Waldemar, ed. *International encyclopedia of ergonomics and human factors*. Vol. 3. Crc Press, 2001.

[34]   Steinhausen, Wilhelm. "Über den Nachweis der Bewegung der Cupula in der intakten Bogengangsampulle des Labyrinthes bei der natürlichen rotatorischen und calorischen Reizung." *Pflüger's Archiv für die gesamte Physiologie des Menschen und der Tiere* 228.1 (1931): 322-328.

[35]   Merfeld, Daniel Michael. *Spatial orientation in the squirrel monkey: an experimental and theoretical investigation*. Diss. Massachusetts Institute of Technology, 1990.

[36]   Ormsby, Charles Clark. *Model of human dynamic orientation*. Diss. Massachusetts Institute of Technology, 1974.

[37]   Fernandez, Cesar, and Jay M. Goldberg. "Physiology of peripheral neurons innervating semicircular canals of the squirrel monkey. II. Response to sinusoidal stimulation and dynamics of peripheral vestibular system." *J Neurophysiol* 34.4 (1971): 661-675.

[38]   Newman, Michael, et al. "Perceptual Modeling as a Tool to Prevent Aircraft Upset Associated with Spatial Disorientation." *AIAA Guidance, Navigation, and Control Conference*. 2014.

[39]   Zupan, Lionel H., Daniel M. Merfeld, and Christian Darlot. "Using sensory weighting to model the influence of canal, otolith and visual cues on spatial orientation and eye movements." *Biological cybernetics* 86.3 (2002): 209-230.

[40]   Hain, Timothy C., T. S. Ramaswamy, and M. A. Hillman. "Anatomy and physiology of the normal vestibular system." *Vestibular Rehabilitation. 2nd ed. Philadelphia, PA: FA Davis Company* (2000).

[41]   Young, Laurence R., and Jacob L. Meiry. "A revised dynamic otolith model." *Aerospace medicine* 39.6 (1968): 606-608.

[42]   Schleppe, John B. *Development of a real-time attitude system using a quaternion parameterization and non-dedicated GPS receivers*. University of Calgary, 1996.

[43]   Dillsaver, Matthew, Carlos Cesnik, and Ilya Kolmanovsky. "Gust Response Sensitivity Characteristics of Very Flexible Aircraft." *AIAA Atmospheric Flight Mechanics Conference, AIAA*. Vol. 4576. 2012.

[44]   Hogge, Edward F. "B-737 Linear Autoland Simulink Model." *NASA, Langley Research Center, Hampton, Virginia, USA, Tech. Rep. CR-2004-213021* (2004).

[45]   Hoblit, F.M., *Gust Loads on Aircraft: Concepts and Applications*, AIAA Education Series, Washington, D.C., 1988.

[46]   Zipfel, Peter H. *Modeling and simulation of aerospace vehicle dynamics*. AIAA, 2000.

[47]   Moorhouse, David J., and Robert J. Woodcock. *Background Information and User Guide for MIL-F-8785C, Military Specification-Flying Qualities of Piloted Airplanes*. No. AFWAL-TR-81-3109. AIR FORCE WRIGHT AERONAUTICAL LABS WRIGHT-PATTERSON AFB OH, 1982.

[48]   Matlab Dryden Wind Turbulence Model (Continuous) <mathworks.com/help/aeroblks/drydenwindturbulencemodelcontinuous.html>

[49]   Schmidt, Louis V. *Introduction to aircraft flight dynamics*. AIAA, 1998.

[50]   Groen, J. J. "Problems of the semicircular canal from a mechanico-physiological point of view." *Acta Oto-Laryngologica* 53.S163 (1961): 59-67.

[51]   Selva, P., "Modeling of the Vestibular System and Nonlinear Models for Human Spatial Orientation Perception," Université de Toulouse, Toulouse, 2009.

[52]   Kynor, D. B., "Disorientation Analysis and Prediction System," Final Report AFRL-HE-WP-TR-2002-0179, United States Air Force Research Laboratory, Wright-Patterson Air Force Base, OH, 2002.